

Department of Physics, Chemistry and Biology

Master's Thesis

Search for Dark Matter in the Upgraded High Luminosity LHC at CERN

Sensitivity of ATLAS phase II upgrade to dark matter production

Sven-Patrik Hallsjö

Thesis work performed at Stockholm University

Linköping, June 4, 2014

LITH-IFM-A-EX--14/2863--SE



Linköpings universitet
TEKNISKA HÖGSKOLAN

Search for Dark Matter in the Upgraded High Luminosity LHC at CERN

Sensitivity of ATLAS phase II upgrade to dark matter production


Sven-Patrik Hallsjö

Thesis work performed at Stockholm University

Linköping, June 4, 2014

Supervisor: **Docent Christophe Clément**
FYSIKUM, Stockholm University
Professor Magnus Johansson
IFM, Linköping University

Examiner: **Professor Magnus Johansson**
IFM, Linköping University

	Avdelning, Institution Division, Department Theoretical physics group Department of Physics, Chemistry and Biology SE-581 83 Linköping	Datum Date 2014-06-04
---	---	--

Språk Language <input type="checkbox"/> Svenska/Swedish <input checked="" type="checkbox"/> Engelska/English <input type="checkbox"/> _____	Rapporttyp Report category <input type="checkbox"/> Licentiatavhandling <input checked="" type="checkbox"/> Examensarbete <input type="checkbox"/> C-uppsats <input type="checkbox"/> D-uppsats <input type="checkbox"/> Övrig rapport <input type="checkbox"/> _____	ISBN _____ ISRN LITH-IFM-A-EX--14/2863--SE <table style="width: 100%;"> <tr> <td style="width: 60%;">Serietitel och serienummer</td> <td style="width: 40%;">ISSN</td> </tr> <tr> <td>Title of series, numbering</td> <td>_____</td> </tr> </table>	Serietitel och serienummer	ISSN	Title of series, numbering	_____
Serietitel och serienummer	ISSN					
Title of series, numbering	_____					

URL för elektronisk version http://urn.kb.se/resolve?urn=urn:nbn:se:liu:diva-XXXXX	
---	--

Titel Title	Sökandet efter mörk materia i den uppgraderade hög luminositets LHC i CERN Search for Dark Matter in the Upgraded High Luminosity LHC at CERN
Undertitel Subtitle	Känslighet för mörk materia produktion hos den fas II uppgraderade ATLAS . Sensitivity of ATLAS phase II upgrade to dark matter production
Författare Author	Sven-Patrik Hallsjö

Sammanfattning Abstract	<p>The LHC at CERN is now undergoing a set of upgrades to increase the center of mass energy for the colliding particles to be able to explore new physical processes. The focus of this thesis lies on the so called phase II upgrade which will preliminarily be completed in 2023. After the upgrade the LHC will be able to accelerate proton beams to such a velocity that each proton has a center of mass energy of 14 TeV.</p> <p>One disadvantage of the upgrade is that it will be harder for the ATLAS detector to isolate unique particle collisions since more and more collisions will occur simultaneously, so called pile-up.</p> <p>For 14 TeV there does not exist a full simulation of the ATLAS detector. This thesis instead uses data from Monte Carlo simulations for the particle collisions and then uses so called smearing functions to emulate the detector responses.</p> <p>This thesis focuses on how a mono-jet analysis looking for different WIMP models of dark matter will be affected by this increase in pile-up rate.</p> <p>The signal models which are in focus are those which try to explain dark matter without adding new theories to the standard model or QFT, such as the effective theory D5 operator and light vector mediator models.</p> <p>The exclusion limits set for the D5 operators mass suppression scale at 14 TeV and 1000 fb^{-1} are 2-3 times better than previous results at 8 TeV and 10 fb^{-1}.</p> <p>For the first time limits have been set on which vector mediator mass models can be excluded at 14 TeV.</p>
-----------------------------------	--

Nyckelord Keywords	ATLAS, Beyond standard model physics, CERN, Dark matter, Effective operator, Elementary particle physics, High energy physics, Mono-jet analysis, Vector mediator, WIMPS.
------------------------------	---

Abstract

The LHC at CERN is now undergoing a set of upgrades to increase the center of mass energy for the colliding particles to be able to explore new physical processes. The focus of this thesis lies on the so called phase II upgrade which will preliminarily be completed in 2023. After the upgrade the LHC will be able to accelerate proton beams to such a velocity that each proton has a center of mass energy of 14 TeV.

One disadvantage of the upgrade is that it will be harder for the ATLAS detector to isolate unique particle collisions since more and more collisions will occur simultaneously, so called pile-up.

For 14 TeV there does not exist a full simulation of the ATLAS detector. This thesis instead uses data from Monte Carlo simulations for the particle collisions and then uses so called smearing functions to emulate the detector responses.

This thesis focuses on how a mono-jet analysis looking for different WIMP models of dark matter will be affected by this increase in pile-up rate.

The signal models which are in focus are those which try to explain dark matter without adding new theories to the standard model or QFT, such as the effective theory D5 operator and light vector mediator models.

The exclusion limits set for the D5 operators mass suppression scale at 14 TeV and 1000 fb^{-1} are 2-3 times better than previous results at 8 TeV and 10 fb^{-1} .

For the first time limits have been set on which vector mediator mass models can be excluded at 14 TeV.

Acknowledgments

I wish to dedicate this thesis to my mathematics teacher Ulf Rydmark without whom I would not have studied physics.

A big thank you to my family, fiancée and friends who have supported me throughout my education. A warm thank you to my friend Joakim Skoog who altered some of the images for me.

I want to thank my supervisor Christophe Clément and all those who helped me at Stockholm University.

I also want to thank my examiner Magnus Johansson, who always took time to answer any question from and support his students.

A special thank you to Professor Irina Yakimenko who was responsible for my profile in physics.

Linköping, June 2014
Sven-Patrik Hallsjö

Contents

42	Notation	ix
43	1 Introduction	1
44	1.1 Research goals	2
45	1.2 Theoretical Background	3
46	1.2.1 Quantum mechanics and quantum field theory	3
47	1.2.2 Nuclear, particle and subatomic particle physics	4
48	1.2.3 The standard model of particle physics	4
49	1.2.4 Dark matter	5
50	1.2.5 Signal models	7
51	1.2.6 Jets	8
52	1.2.7 Search for WIMPS	9
53	1.3 Experimental overview	10
54	1.3.1 LHC	10
55	1.3.2 ATLAS	11
56	1.3.3 Coordinate system	12
57	1.3.4 Pile-up	12
58	1.3.5 Mono-jet analysis	13
59	1.3.6 Phase II high luminosity upgrade	14
60	1.3.7 Monte Carlo simulation	15
61	2 Validation of smearing functions	17
62	2.1 Smearing functions	18
63	2.1.1 Electron and photon	20
64	2.1.2 Muon	20
65	2.1.3 Tau	20
66	2.1.4 Jets	20
67	2.1.5 Missing Transverse Energy	21
68	2.2 Validation	22
69	2.2.1 Method	22
70	2.3 Results	23
71	2.3.1 Electron and photon	24
72	2.3.2 Muon	25

73	2.3.3	Tau	25
74	2.3.4	Jets	26
75	2.3.5	Missing Transversal Energy	27
76	2.3.6	Summary	28
77	2.4	Discussion	29
78	2.4.1	Dependence of smearing on pile-up	29
79	2.4.2	Comparison to expected results	29
80	2.5	Conclusion	29
81	3	Sensitivity to dark matter signals	31
82	3.1	Signal over background	32
83	3.1.1	Signal Region	32
84	3.1.2	Cross section and luminosity weighting	32
85	3.1.3	Background processes	33
86	3.1.4	Verification of background normalisation	33
87	3.1.5	Errors in background	34
88	3.1.6	Figure of merit	35
89	3.1.7	D5 operator models	35
90	3.1.8	Light vector mediator models	36
91	3.2	Signal regions	37
92	3.2.1	Signal region definitions	37
93	3.2.2	Verifying background data	38
94	3.3	Results	39
95	3.3.1	Verifying background data	39
96	3.3.2	Signal and background events in signal regions	39
97	3.3.3	Project exclusion limits on M^*	41
98	3.3.4	Projection exclusion limits on mediator mass models	43
99	3.4	Discussion	46
100	3.4.1	Comparison to previous results	46
101	3.4.2	Effect of the high luminosity	46
102	3.5	Conclusion	47
103	3.5.1	Limit on M^*	47
104	3.5.2	Limit on mediator mass models	47
105	3.5.3	Effect of the high luminosity	47
106	4	Final remarks	49
107	A	Datasets	53
108	A.1	Background processes	53
109	A.1.1	Validation	53
110	A.1.2	Background for signals	54
111	A.2	Signals	54
112	A.2.1	Q_{cut}	54
113	A.2.2	D5 signal processes	54
114	A.2.3	Light vector mediator processes	54
115	Bibliography		59

116
117

Notation

NOTATIONS

118

Notation	Explanation
barn(b)	1 barn(b)= 10 ⁻²⁴ cm ²
\oplus	$a \oplus b = \sqrt{a^2 + b^2}$, $a \oplus b \oplus c = \sqrt{a^2 + b^2 + c^2}$

ABBREVIATIONS

119

Abbreviation	Expansion
ATLAS	A large Toroidal LHC ApparatuS
CERN	Organisation européenne pour la recherche nucléaire ¹
CMS	Compact Muon Solenoid
CR	Control Region
LHC	Large Hadron Collider
MC	Monte Carlo
SM	the Standard Model of particle physics
SR	Signal Region
WIMP	Weakly Interacting Massive Particle
WIMPS	Weakly Interacting Massive ParticleS
QED	Quantum ElectroDynamics
QFT	Quantum Field Theory
QM	Quantum Mechanics

¹Originally, Conseil Européen pour la Recherche Nucléaire

1

Introduction

Discrepancies in measurements of the rotations of galaxies indicate the presence of a large amount of matter which interacts through gravity, though not electromagnetically making it invisible to all telescopes that exist today. This matter is commonly referred to as dark matter. Since no known or hypothesized particle in the standard model of particle physics can be used as a candidate for dark matter, this hints at the presence of new physics.

At the Organisation Européenne pour la Recherche Nucléaire (CERN) focus lies among other things to discover any evidence of so called weakly interacting massive particles (WIMPS) which may be a candidate for dark matter. It is impossible to electromagnetically detect any interaction of dark matter candidates on the subatomic scale. However through using existing theoretical frameworks as templates, searches can be designed. This is done by searching for assumed decay channels by investigating what is invisible to the ATLAS and CMS detectors and by using momentum conservation. Through this it is hoped that signs will be found. Though to date no candidates for WIMPS have been found nor any other explanation of dark matter.

Current experiments at CERN and current theories now show that higher energies are required at the LHC to be able to see any signs of WIMPS. This is why the LHC and all detectors at CERN are undergoing a vast upgrade program [1]. In this thesis focus will be on the last part of the upgrade due for completion in 2023, known as the high luminosity-LHC phase II upgrade; and also on the ATLAS detector. The method used in this thesis focuses on looking at data which emulate conditions at the upgraded LHC.

1.1 Research goals

This research took place at Stockholm University from January 7th until May 16th. During the research period the following tasks were set up and performed or answered:

- Implement a C++ programme that loops over the collisions inside the signal and background datasets.
- For each collision retrieve the relevant observables (variables used to extract the signal over the background) and apply "smearing functions" to emulate the effect of the high luminosity on the observables.
- For both signal and background datasets, compare observables before and after smearing. What observables are the least/most affected?
- Implement selection criteria that select the signal collisions efficiently while significantly reduce the background. In a first step the selection criteria should be taken from existing studies.
- Selection criteria can be evaluated and compared with each other using a figure of merit p , that measures the sensitivity of the experiment to the dark matter signal. Calculate p for the given selection criteria before and after smearing.
- What is the effect of the high luminosity (smearing) on the value of p ?
- Investigate other selection criteria and observables, to mitigate the effect of high luminosity. Use p to rank different criteria after smearing.
- Conclude on the effect of the high luminosity on the sensitivity for dark matter and possible ways to mitigate its effects using alternative observables and selection criteria.

1.2 Theoretical Background

1.2.1 Quantum mechanics and quantum field theory

In the beginning of the 20th century, some physical phenomena could not be explained by classical physics, for example the ultra-violet disaster of any classical model of black-body radiation or the photoelectric effect [2]. It was these phenomena that led to the formulation of quantum mechanics (QM), where energy transfer is quantized and particles can act as both waves and particles at the same time [2, 3].

Combining QM with classical electromagnetism proved harder than expected, calculating the collision of a photon(em-field) and an electron (particle/wave) is tricky. This can be seen when trying to calculate the scattering between them both in a QM schema. One idea that came from this was to explain them both in the same framework, field theory. Also trying to incorporate special relativity into QM suggested a field description where space-time is described using the metric formalism from differential geometry. The culmination of both of these problems is the first part of a Quantum field theory (QFT), Quantum electrodynamics (QED) which with incredible precision explains electromagnetic phenomena including effects from special relativity [4]. It is in this merging that antimatter was theorised, since it is a requirement for the theory to hold. After the discovery of antimatter QED was assumed to give a correct description of the phenomena around us. Since then the theory has been altered somewhat to explain more and more experimental data. This is discussed more in subsection 1.2.2 and subsection 1.2.3.

To be able to calculate properties in QFT one uses the Lagrangian formalism [5], which gives a governing equation for different physical processes. In general the Lagrangian used for the standard model is quite complicated, however one can focus on one of the different terms corresponding to a specific interaction. This can be done to calculate the so called cross-section for a process.

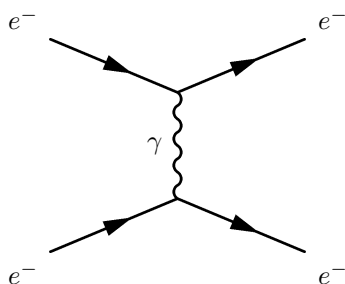


Figure 1.1: An example of a Feynman diagram explaining an electron-electron scattering using QED.

For a particle collision [6], the cross-section can be seen as a measure of the effective surface area seen by the impinging particles and as such is expressed in units of area. The cross section is proportional to the probability that an interaction will occur. It also provides a measure of the strength of the interaction between the scattered particle and the scattering center. A step to simplify the

calculation of the cross-sections is to use so called Feynman diagrams, an example of which is given in figure 1.1. Through the figure, which comes with certain rules, and knowing what the major process is (in this case QED) one can calculate the cross-section [4, 6]. It is this which is needed to predict the detection of new particles.

1.2.2 Nuclear, particle and subatomic particle physics

Many could argue that these branches of physics started after Ernest Rutherford's famous gold foil experiment [7], where he discovered that atoms are composed of a nucleus, a lot of empty space and electrons.

It was this discovery that sparked the curiosity to see what the nucleus is made of and what forces govern the insides of atoms. After this, and the combination of the theoretical description given by QM, a lot more has been discovered and still more has been predicted. The newest of these is of course the Higgs particle, which was predicted through QFT and then discovered by the ATLAS and the CMS experiments at CERN [8, 9].

It is now known that all discovered particles are built up of fundamental particles, these build up the standard model [7].

1.2.3 The standard model of particle physics

To date there are two fundamental types of particles which are modelled as point like, quarks and leptons, seen in figure 1.2. Aside from this and also seen in the figure are the gauge bosons which are mediators of the different forces.

All other known particles are built up by these fundamental particles. Combined particles are often divided into different groups depending on the fundamental particles that constitute them. For instance particles built up of three quarks are known as hadrons, particles with an integer spin are known as bosons whereas half-integer particles are known as fermions.

The standard model of particle physics, referred to simply as the standard model (SM) categorizes all the fundamental particles that have been discovered experimentally. QFT explains the interactions between these particles and it has also predicted several particles by including symmetries [7].

SM is today the pinnacle of particle physics and can be used to explain almost everything that occurs around us. There are however some problems [11]:

- There is no link between gravity and the SM.
- Asymmetry between matter and antimatter can not be fully explained.
- No explanation for dark matter.

In this thesis focus lies with dark matter; some more introduction to possible dark matter candidates in extensions to SM are explained in subsection 1.2.4.

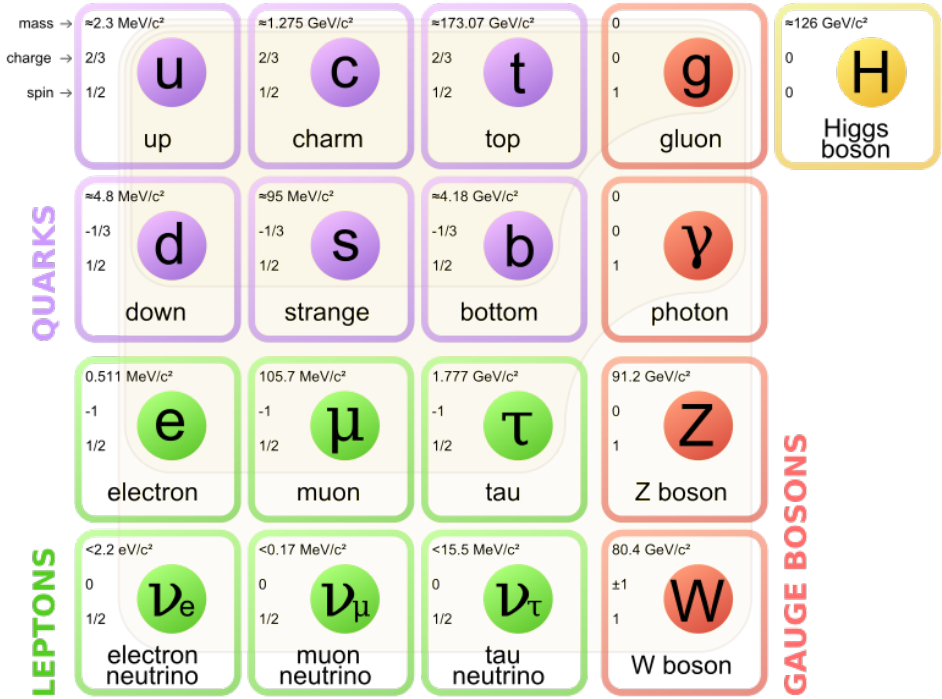


Figure 1.2: The standard model of particle physics where the three first columns represent the so called generations, starting with the first [10].

1.2.4 Dark matter

Dark matter is the name given to, among other things, the solution to the discrepancies of galactic rotations [12].

The presence of dark matter can be measured indirectly from its gravitational effects. Focus on matter in a galaxy which is rotating around the center of the galaxy. Through Newton's law of gravity and the centrifugal force one can calculate the rotation speed as a function of the distance to the center of the galaxy. Since one of these forces is attractive and the other repulsive, if the matter is in a stable orbit around the galactic center they must be equal and give us an expression for the speed depending on the distance. Newton's law and the centrifugal force can be written as:

$$F_{Gravitational} = G \frac{Mm}{r^2} \equiv G_M \frac{m}{r^2} \quad F_{Centrifugal} = m \frac{V^2}{r} \quad (1.1)$$

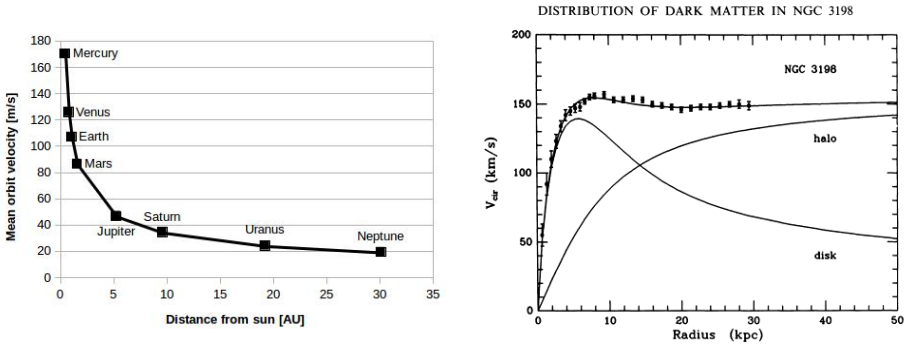
where G is the gravitational constant, M the mass of the centre object, m the mass of the matter, r the distance between the two and V is the rotation speed. It has been simplified using G_M since all matter orbits the same galactic center. The assumption that the two objects have spherical symmetrical mass distributions

and that the rotating object is in a circular orbit outside of the center object have been made. Setting the equations in (1.1) equal result in:

$$G_M \frac{m}{r^2} = m \frac{V^2}{r} \Leftrightarrow V^2 = \frac{G_M}{r} \Rightarrow V = \sqrt{\frac{G_M}{r}} \propto \frac{1}{\sqrt{r}} \quad (1.2)$$

where V is assumed to be positive and \propto denotes proportionality. Through these simple calculations it is shown that the rotation speed should decrease with an increased distance. The same reasoning can be applied to our solar system where this is the case, see figure 1.3a. The relation for our solar system is in these units $V = \frac{107}{\sqrt{r}}$ where 107 can be used in (1.2) to calculate the mass of the sun.

When applying the same reasoning to galaxies the rotation speed does not decrease with an increased distance! In figure 1.3b experimental data can be seen from the galaxy NGC3198 with a fitted curve which does not decrease with the distance but is instead constant. This is the discrepancy which is solved by postulating the existence of dark matter [13]. After this the big question arises, what



(a) Rotation speed of planets in our solar system. Since the distance is quite small on an astronomical scale, there is no sign of dark matter. Based on data from Ref. [14].

(b) Rotation speed of matter in NGC3198 with a curve fitting and three different models, if only a dark matter halo existed, if there was no dark matter and the correct, if both exist [15].

Figure 1.3: Different rotation curves, both for planets in our solar system and matter in the NGC3198 galaxy.

could dark matter consist of? What is known so far lies in the name. It is called dark since there is no electromagnetic interaction, and matter since it has gravitational interaction. This means that it can not be made up of anything in the Standard Model apart from neutrinos or the higgs boson. Astrophysical measurements have also indicated that dark matter can not be fully explained as being neutrinos nor baryonic matter [16]. The requirement of a stable dark matter particle excludes the higgs boson as a candidate. This means that dark matter can not be made out of any standard model particles.

The main interest of this thesis and also the main contributor to the rotational discrepancies is known as cold dark matter. This is due to the matter having a low speed, thus low kinetic energy, and have a high particle mass (In the GeV scale) [11, 17, 18]. There are several strategies to search for dark matter [11].

- Ordinary matter interacting with ordinary matter can produce dark matter, known as production. This is the process which occurs in particle accelerators and is the method explored in this thesis.
- Dark matter interacting with ordinary matter can produce dark matter, known as direct detection.
- Dark matter interacting with dark matter can produce ordinary matter, known as indirect detection.

In this thesis the focus lies with production at colliders, namely the LHC. There are several theoretical models for how to detect dark matter in proton-proton collisions such that occur at the LHC at CERN. This is covered more in subsection 1.2.7.

1.2.5 Signal models

In quantum field theory the objective is usually to find the part of the Lagrangian which explains a type of interaction, known as the operator of the interaction and also to find the probability amplitude (cross-section) for a certain interaction. For complicated processes it is easier to employ a simplified phenomenological model. This is done by using an effective field theory and the concept is explained in figure 1.4. The operator can be found through assuming the possible interactions and using the effective field theory [4].

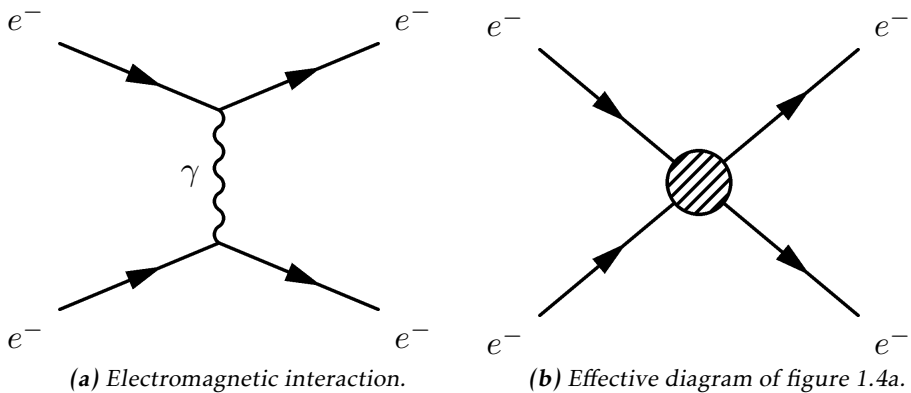
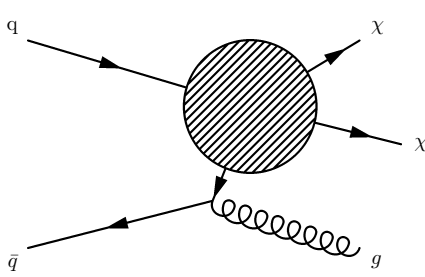


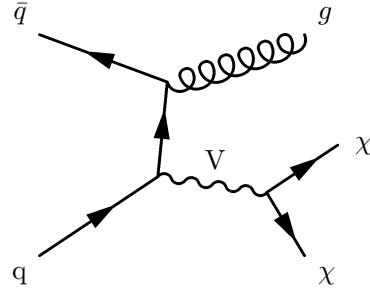
Figure 1.4: Feynman diagram of an electron-electron scattering, both as a diagram where a photon is exchanged and as its effective theory version, where the details are hidden in the blob.

In this thesis the same effective field theory as in Refs. [17, 19] is considered, denoted D5 and explained in figure 1.5a. The WIMP (denoted χ) is assumed to be the only particle in addition to the standard model fields and is assumed to interact through the electroweak force. In order to explain dark matter the WIMP χ must be stable, for this reason only Feynman diagrams with an even number of χ are considered. It is assumed that the mediator is heavier than the WIMPs, meaning that the mediator interactions are in higher order terms of the effective field theory and thus not included in the operators. In this work WIMPs are assumed to be Dirac fermions (half integer spin and is not its own antiparticle).

Another model which is considered is a vector mediator model which is described by figure 1.5b. This model is based on the assumption that the interaction of WIMPs is mediated by a particle denoted V which is a spin 1 particle and thus a vector mediator. This particle is modelled as a heavy Z-boson which governs the electroweak interactions. The free parameters of this mediator particle are its weight and its width which is related to the lifetime of the particle and which decay modes exist.



(a) Effective Feynman diagram explaining the D5-operator.



(b) Feynman diagram describing the vector mediator model.

Figure 1.5: Feynman diagrams describing the signal models used in this thesis.

1.2.6 Jets

In particle collisions free gluons and quarks with high energy can be produced. According to QFT these can not exist and must decay through a process known as hadronization meaning that they will decay into a cone of energetic hadrons, which is known as a jet. It is not possible to measure these free gluons or quarks, however this cone of hadrons will travel in the same direction and will be measured by the calorimeters, see subsection 1.3.2. These measurements can then be summed to calculate the energy and momentum which the initial gluon or quark had which in turn results in more information about the collision.

1.2.7 Search for WIMPS

The main problem with searching for WIMPS is that one is looking for a small signal among a lot of uninteresting proton-proton collisions. One way to search for WIMPS and overcome this difficulty is a so called mono-jet analysis which is described in subsection 1.3.5.

This method is a way to detect WIMP production among other proton-proton collision events and relies on the observation of a high energetic jet, which arises from the gluon in both figures in figure 1.5, on one side and seemingly non conservation of energy or momentum, which will be denoted missing energy. This means that something has happened which the detectors can not detect. If the models from subsection 1.2.5 can explain the missing energy, then evidence for WIMP production would have been found.

Since the search for WIMPS at the LHC is based on looking at the missing energy, not actual detection, the experiment can not establish if a WIMP is stable on a cosmological time scale and thus if it is a dark matter candidate [18]. This means that if a candidate is found, it may still not be the dark matter that is needed to explain the cosmological observations.

ATLAS has looked at proton-proton collisions, with 8 TeV center of mass energy, which contain high energetic jets without finding any excess of mono-jet events. This is why it is very interesting that the LHC is undergoing an upgrade that will allow higher energy levels, see subsection 1.3.6. With this collisions can be given higher energy and thus the produced particles can be comprised of higher mass which may produce more mono-jet events [1].

1.3 Experimental overview

1.3.1 LHC

The large hadron collider (LHC) is a particle accelerator located at CERN near Geneva in Switzerland, see figure 1.6. The accelerator was built to explore physics beyond the standard model and to make more accurate measurements of standard model physics. Before it was shut down for an upgrade in 2012 it was able to accelerate two proton beams to such a velocity that each proton in them had an energy of 4 TeV which gives a center of mass energy of $\sqrt{s} = 8$ TeV. The proton beam is comprised of bunches of protons with enough spacing that bunch collisions can happen independent of each other. The rate at which the accelerator produces a certain process can be calculated through the instantaneous luminosity. For the LHC the instantaneous luminosity was $10^{34} \text{ cm}^{-2}\text{s}^{-1}$ [20] or $10\text{nb}^{-1}\text{s}^{-1}$ where $1 \text{ barn(b)} = 10^{-24} \text{ cm}^2$.

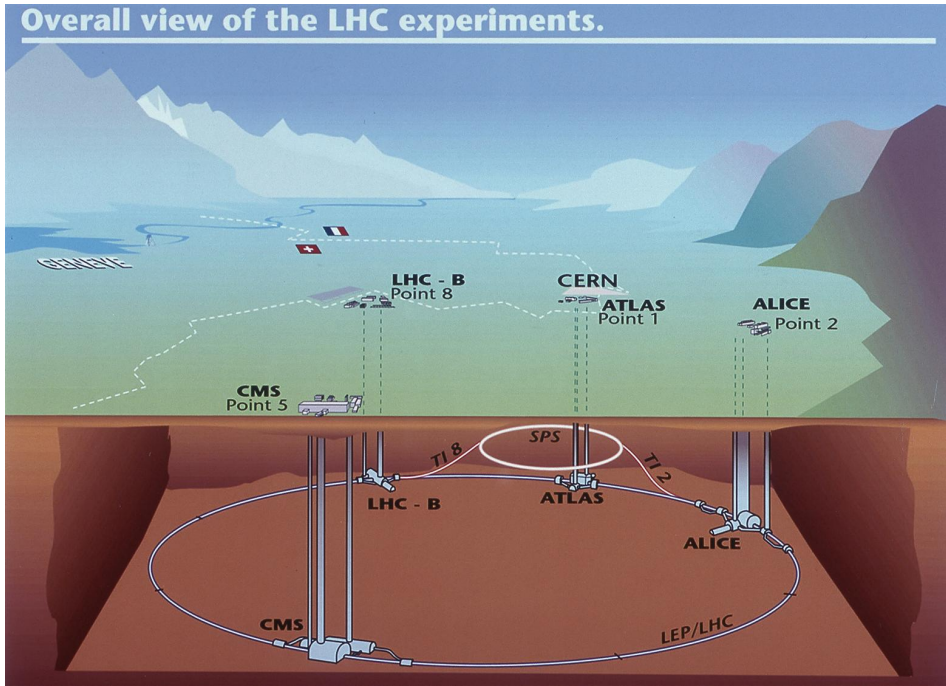


Figure 1.6: The LHC and the different detector sites [21].

The instantaneous luminosity, often just denoted luminosity, can be defined in different ways depending on how the collision takes place. For two collinear intersecting particle beams it is defined as:

$$\mathcal{L} = \frac{fkN_1N_2}{4\pi\sigma_x\sigma_y} \quad (1.3)$$

where N_i is the number of protons in each of the bunches, f is the frequency at which the bunches collide, k the number of colliding bunches in each beam, and σ_x (σ_y) is the horizontal (vertical) beam size at the interaction point. Since the instantaneous luminosity increases quadratically with more protons in each bunch, increasing the number of protons would be a good strategy to increase the instantaneous luminosity. However aside from the difficulties to create and maintain a beam with more particles, a large N_i increases the probability for multiple collisions per bunch crossing, referred to as pile-up. Pile up will be a key aspect which is described more in subsection 1.3.4.

The expected number of events for a given physical process can be calculated by using the instantaneous luminosity (1.3) through the following:

$$N = \sigma \int \mathcal{L} dt \equiv \sigma \mathcal{L} \quad (1.4)$$

where \mathcal{L} is the integrated luminosity and σ is the cross section which is often measured in barn. The integrated luminosity is a measurement of total number of proton-proton interactions that have occurred over time and is also a common measure of how much data was recorded. Before the LHC was shut down \mathcal{L} was 20.8 fb^{-1} .

1.3.2 ATLAS

As seen in figure 1.6, there are several detectors at the LHC. One of these is ATLAS which is a general purpose detector that uses a toroid magnet. Its goal is to observe several different production and decay channels. The detector is composed of three concentric sub-detectors, the Inner detector, the Calorimeters and the Muon spectrometer [22].

The Inner detector's main task is to measure the tracks of the particles and measure the position of the initial proton-proton collision. Aside from this it measures the track momenta and the charge of charged particles. It can however only detect charged particles.

The Calorimeters, electromagnetic and hadronic, are used to measure the energy contained in the different particles. The electromagnetic calorimeter is used to measure energy and direction of photons and electrons, whereas the hadronic calorimeter is designed to measure the energy and direction of hadrons.

The Muon spectrometer is used to measure signs of muons, which will simply pass through the other detectors without leaving a trace. It also measures the energy and momentum of the muons.

Neutrinos escape the ATLAS experiment without being detected, and in this thesis it is assumed that WIMPS pass through all the detectors without leaving any trace. Therefore WIMPS and neutrinos have the same detector signature. As seen in section 3.3 the main background to the WIMP signal is the production of a Z-boson that in turn decays to two neutrinos mimicking the WIMP signature.

1.3.3 Coordinate system

The coordinate system of ATLAS, seen in figure 1.7, is a right-handed coordinate system with the x -axis pointing towards the centre of the LHC ring, the z -axis along the tunnel/beam (counter clockwise) seen from above and the y -axis points upward. The origin is defined as the geometric center of the detector. A cylindrical coordinate system is also used for the transverse plane, (R, φ, Z) . For simplicity the pseudorapidity of particles from the primary vertex is defined as:

$$\eta = -\ln\left(\tan \frac{\theta}{2}\right) \quad (1.5)$$

where θ is the polar angle (xz -plane) measured from the positive z -axis. The difference in η of two particles is through this definition invariant under Lorentz boosts in the z -direction.

It is quite common to calculate the distance between particles and jets in the (η, φ) space, $d = \sqrt{(\Delta\eta)^2 + (\Delta\varphi)^2}$.

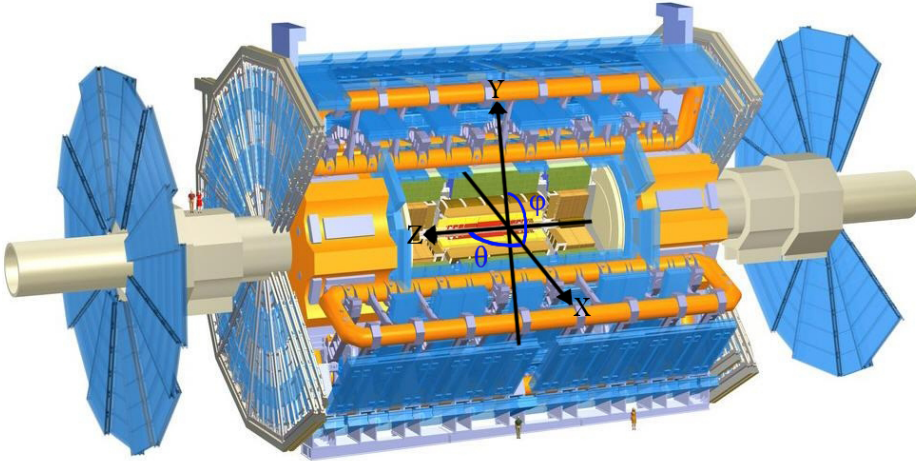


Figure 1.7: The ATLAS detector and the definition of the orthogonal Cartesian coordinate system. Image altered from Ref. [23].

1.3.4 Pile-up

Pile-up is the phenomenon that several proton-proton collisions occur simultaneously. The number of pile-up is defined as the average number of proton-proton collisions that occur per bunch crossing per second and is denoted as $\langle\mu\rangle$. The value of μ can be calculated by adjusting a Poisson distribution to fit the curve created by the number of interactions per bunch crossing at a given luminosity. When this is done μ will be the mean value of the Poisson distribution. The value of μ will be higher after the proposed upgrade compared to now, see section 1.3.6, which may decrease the detector performance.

1.3.5 Mono-jet analysis

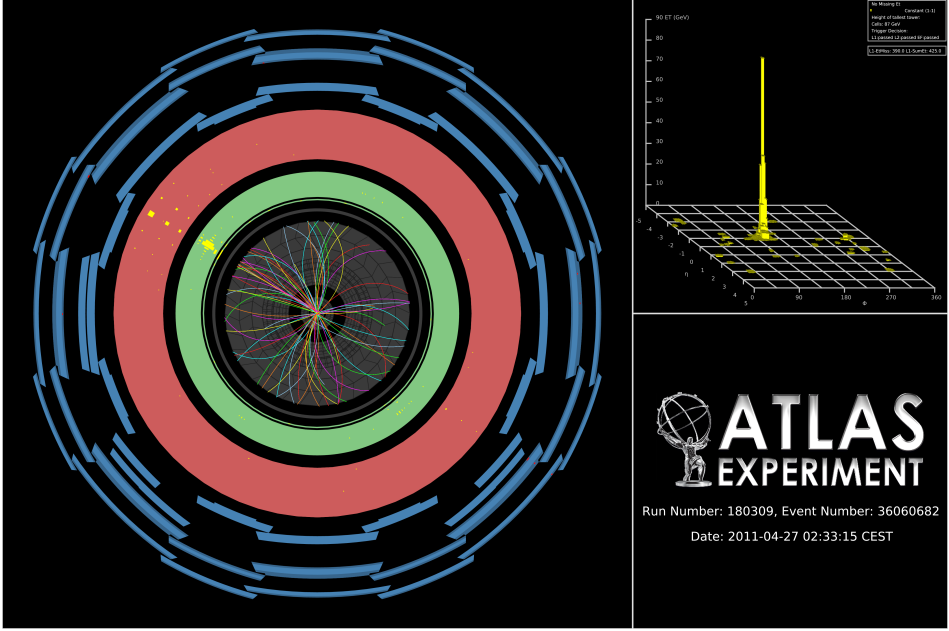


Figure 1.8: Image in the transverse plane of a mono-jet event recorded by the ATLAS experiment [24]. The figure in the top right is a diagram in the (η, ϕ) -plane showing where in the calorimeter (red in the main figure) the energy is deposited and how much.

When measuring the transverse energy one can in some interactions find inconsistencies such as jets, discussed in subsection 1.2.6, that are in excess in one direction. Conservation of momentum in the transverse plane of the experiment indicates that the sum of all momenta should be zero as before the collision. In figure 1.8 one can see a high energetic jet which gives an excess of transverse energy in one direction after the collision. Since there is no balancing jet there must be transverse energy that is not detected, denoted E_T^{Miss} , indicating that the energy to balance this can not be detected. This could for instance be neutrinos or the characteristic signature of WIMPS.

E_T^{Miss} is the modulus of the \vec{E}_T^{Miss} vector which is defined as:

$$\vec{E}_T^{Miss} = - \sum \vec{p}_T^{Jet} - \sum \vec{p}_T^{Electron} - \sum \vec{p}_T^{Muon} - \sum \vec{p}_T^{Tau} - \sum \vec{p}_T^{Photon} \quad (1.6)$$

where p_T denotes the transverse momenta. There are two main classes of events, signal and background. The signal corresponds to events that would arise from one of the processes in subsection 1.2.5. However to know that the missing energy is a sign of the signal then one must understand all the other components that could contribute to the missing energy. Also there must be an excess of miss-

ing energy from what is expected from the background, since is it comprised of standard model processes that can mimic the mono-jet signature.

1.3.6 Phase II high luminosity upgrade

At the moment, the whole LHC is undergoing a step by step upgrade program which will be finalized around 2022-2023, denoted the high luminosity upgrade, or HL-upgrade. The upgrade consists of different stages, meaning that the upgrade will halt for periods so that experiments can take place. In figure 1.9 one

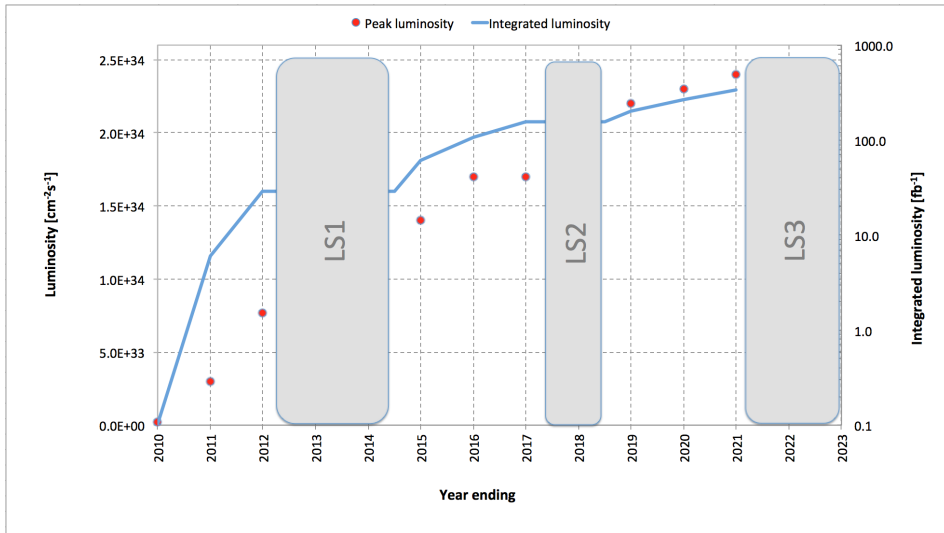


Figure 1.9: A graph showing the upgrading timetable with the instantaneous luminosity, denoted peak luminosity, and integrated luminosity expected in the different stages.

can see the three proposed upgrades. The period after LS1 is denoted phase 0, after LS2 phase I and after LS3 phase II.

LS1 is the upgrade which will take the LHC to its designed performance.

LS2 will push the LHC to the ultimate designed center of mass energy and instantaneous luminosity without too dramatic changes to the accelerator.

LS3, which is the focus of this thesis, will increase the center of mass energy and instantaneous luminosity even more. Though for this to happen a modification of the whole LHC must be done.

The following is expected for the experiments done after phase II:

Entity	Expected (2023)	Last run (2012)
Instantaneous luminosity	$\mathcal{L} \sim 50 \text{ nb}^{-1} \text{ s}^{-1}$	$\mathcal{L} \sim 10 \text{ nb}^{-1} \text{ s}^{-1}$
Integrated luminosity	$\mathcal{L} = 1000 - 3000 \text{ fb}^{-1}$	$\mathcal{L} = 20 \text{ fb}^{-1}$
Pile-up	$\langle \mu \rangle = 140$	$\langle \mu \rangle = 20$
Center of mass energy	$\sqrt{s} = 14 \text{ TeV}$	$\sqrt{s} = 8 \text{ TeV}$

Table 1.1: Expected running values for the Phase II HL-upgraded LHC with older values for comparison [25].

Where it should be noted that the integrated luminosity indicates the total amount of data which will be collected after the upgrade is completed before the next upgrade takes place.

1.3.7 Monte Carlo simulation

As mentioned before, in this thesis only emulated data was used. This data is created by using a Monte Carlo (MC) simulation of the background processes and the expected signal. To do this a program called MadGraph is used.

MadGraph [26] starts with Feynman diagrams and then generates simulated events based on lots of different parameters. This generator was used to generate signal samples used in this thesis.

Sherpa [27] is very similar to MadGraph and was used to generate the background samples used in this thesis.

PYTHIA [28] is a package which adds the correct description of jets to MadGraph by including hadronization. The correct description of pile-up comes from other ATLAS software.

The tool to access all this data and analyse it is a tool called ROOT, which is used for programming high energy physics related tools [29].

Validation of smearing functions

A full detector simulation of the ATLAS detector based on the GEANT [30] program makes it possible to obtain the expected detector responses to electrons, muons, tau leptons, photons (γ) and jets of hadrons. However these simulations are extremely time-consuming and require a lot of computing power. Also at the present time only a limited set of these simulations exists for the ATLAS phase II upgrade. In this thesis a different strategy is used.

Instead of performing a full detector simulation of the observed particles from the event generator, which simulates the proton-proton collisions, have their energy and momenta values smeared up or down by using a probability distribution following resolution functions specific for each type of particle. The resolution functions emulate how the detector and the reconstruction are affected by the increased luminosity and the pile-up which comes with this.

The resolution functions or smearing functions are the official functions developed from previous studies [1, 31] by the ATLAS collaboration for the study of the ATLAS phase II upgrade. The key result of those studies was that the direction of the momenta is unaffected and that only jets and E_T^{Miss} are affected by pile-up. Since this was confirmed in previous studies it was not incorporated into the smearing functions as discussed more in section 2.1.

Since part of this thesis work is to take the official ATLAS smearing functions and apply the smearing to each particle, it is important to check that the energy and momenta resolutions of the smeared objects are consistent with the expected values. Thus in this chapter the energy and momenta resolutions are measured after applying the smearing to some simulated processes and the resulting resolutions are compared with the expected values.

2.1 Smearing functions

In a simulation of a proton-proton collision all quantities such as energy, momentum and direction of all produced particles are perfectly known. In a real experiment it is only possible to get measured values from the detector. The detector energy and momentum resolutions given in the smearing functions relate the measured values to the true values on a statistical basis as:

$$E' = E + \Delta E \equiv E + \sigma \quad (2.1)$$

where E is the energy at a truth level and E' is the smeared energy and ΔE or σ is a random number obtained by sampling a Gaussian distribution with mean value 0 and a standard deviation equal to the resolution for that particle, and will be denoted σ and not cross-section as in chapter 1.

The smearing functions are designed so that they take into account the efficiency of the different detectors, how they are constructed as well as their dependence on pile-up. To emulate the measured energies and momenta, the true values are smeared using the known detector resolutions given in table 2.1 which is taken from [31].

Some terminology which is used:

- Energy and momenta before smearing, simulated data, is denoted at a truth level or truth data. The truth data is energy and momenta for particles directly from a Monte Carlo simulation of an event with no detector effects at all.
- Data after smearing, which is comparable to what is measured is denoted as reconstructed data. Reconstruction is the procedure of taking electrical signals from the detectors and from these identifying particles with a specific energy and momenta. In this thesis however this is seen as equivalent to data after smearing.
- In this thesis p_T denotes the transverse momenta, E the energy and μ the pile-up value.

Observable	Absolute σ
Electron & photon	$\sigma = 0.3 \oplus 0.1\sqrt{E(\text{GeV})} \oplus 0.01E(\text{GeV}), \eta < 1.4$ $\sigma = 0.3 \oplus 0.15\sqrt{E(\text{GeV})} \oplus 0.015E(\text{GeV}), 1.4 < \eta < 2.47$
Muon momentum	$\sigma = \frac{\sigma_{id}\sigma_{ms}}{\sigma_{id} \oplus \sigma_{ms}}$ $\sigma_{id} = p_T(a_1 \oplus a_2 p_T)$ $\sigma_{ms} = p_T(\frac{b_0}{p_T} \oplus b_1 \oplus b_2 p_T)$
Tau energy	$\sigma = (0.03 \oplus \frac{0.76}{\sqrt{E(\text{GeV})}})E(\text{GeV}), \text{ for 3 prong.}$
Jet momentum	$\sigma = p_T(\text{GeV})(\frac{N}{p_T} \oplus \frac{S}{\sqrt{p_T}} \oplus C)$ where $N = a(\eta) + b(\eta)\mu$
E_T^{Miss}	$\sigma = (0.4 + 0.09\sqrt{\mu})\sqrt{\sum E(\text{GeV}) + 20\mu}$

Table 2.1: Expected absolute σ where the parameters are given for muons in table 2.2 and for jets in table 2.3. The subscripts *id* and *ms* for the muon momentum resolution denote the parametrisation of the inner detector and the muon spectrometer. The definition of 3 prong for tau can be found in subsection 2.1.3. Functions take from Ref. [31].

From the formulation of the smearing functions in table 2.1, the biggest effect should be seen at low energies. This is related to the difficulty for the hardware triggers to select events. This means that one drawback of the high luminosity upgrade is that very low energy signal regions will be lost.

	a_1	a_2	b_0	b_1	b_2
$ \eta \leq 1.05$	0.01607	0.000307	0.24	0.02676	0.00012
$ \eta > 1.05$	0.03000	0.000387	0.00	0.03880	0.00016

Table 2.2: Parameters used in the muon smearing function taken from Ref. [31].

$ \eta $	a	b	S	C
0-0.8	3.2	0.07	0.74	0.05
0.8-1.2	3.0	0.07	0.81	0.05
1.2-2.8	3.3	0.08	0.54	0.05
2.8-3.6	2.8	0.11	0.83	0.05

Table 2.3: Parameters used in the jet smearing function taken from Ref. [31].

2.1.1 Electron and photon

The identification of electrons relies on finding a hit pattern in the electromagnetic calorimeter which is consistent with that of an electron or a photon.

If there is a track from the inner detector which can be combined with a hit then an electron has been detected. Pile-up will affect the electrons by decreasing the efficiency to identify an electron because of the increased number of tracks. However for the identified electrons the energy resolution will be close to that without pile-up.

Photons are detected similarly to the electron though with an absence of a track and will thus be affected by pile-up similarly to the electron.

The electron and photon have the same smearing since both of their energies are measured in the electromagnetic calorimeter.

2.1.2 Muon

The identification of muons relies on isolated tracks in the inner detector being matched with information in the muon system. Since the muon system is the outermost detector seen from the collision point the effects of pile-up are negligible.

2.1.3 Tau

Tau is detected similarly to the electron. In this thesis all tau processes are for simplicity assumed to be at 3 prong, where prong refers to the number of tracks from which they were reconstructed. Such as tau decaying to 3 pions and a tau neutrino. $\tau^- \rightarrow \pi^- \pi^- \pi^+ \nu_\tau$

This in turn means that the effect of pile-up will be worse compared to an electron as a triplet must be found in an increased number of tracks.

2.1.4 Jets

Jets as described in subsection 1.2.6 are cones of hadronic particles.

The largest effect of pile-up is to add additional jets in the ATLAS detector. These additional jets contribute to additional energy deposited inside the existing jets and to E_T^{Miss} .

2.1.5 Missing Transverse Energy

E_T^{Miss} , the missing transverse energy, which was discussed in subsection 1.3.5, and defined in (1.6), is calculated by knowing that there should be momentum conservation in the collision. It should be affected by pile-up as described in subsection 2.1.4.

2.2 Validation

Validation is the procedure of comparing an expected resolution σ with the resolution measured from the smeared Monte Carlo simulation. Measuring the resolution on the smeared objects uses that E' and E is known which through (2.1) can be used to statistically calculate σ . The comparison is done with Ref. [31] where the resolution depending on energy, momenta and pile-up value is given in table 2.5. The Monte Carlo simulated processes used are listed in table 2.4.

Table 2.4: *Different processes from where data has been taken. Each sample is a simulation of a physical process, the simulation names can be found in appendix A.1.*

Particle	Process
Electron	$W \rightarrow e \nu$
Muon	$W \rightarrow \mu \nu$
Tau	$W \rightarrow \tau \nu$
γ	$\gamma + \text{jet sample}$
Jets	jet sample
E_T^{Miss}	$Z \rightarrow \nu \nu + \text{jet sample}$

2.2.1 Method

The energy and momentum resolutions are obtained for each type of particle by comparing the values before and after smearing.

Fitting a Gaussian curve of the smeared data from a given truth energy or momenta value will then result in the standard deviation which is used in the validation. The standard deviation is also known as the resolution of the data and will be denoted σ and not cross-section as in chapter 1.

The standard deviation is then compared to previous results [31].

The method is presented step by step below:

- Take a MC sample with a given particle, i.e electrons.
- Choose electrons which have a truth energy of 75 GeV.
- Plot the smeared electron energy for this value of truth energy. These plots are given for electrons and photons in figure 2.1.
- Fit a gauss function to the distribution of smeared energy and from this retrieve the sigma value of the fit.
- Compare the measured sigma to the expected resolution given from the smearing functions.

2.3 Results

As discussed above, the method was to plot the data against its smeared counterpart and through this determine σ to see if it conforms to the expected values.

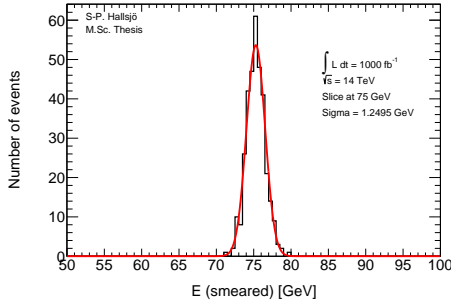
Only one energy or momenta value is shown for simplicity, though the comparison was done for different energy values. The energy is denoted E and in the figures momenta is denoted P_T for transverse momenta.

The average number of pile-up, explained in subsection 1.3.4, is fixed at 60 as a benchmark unless anything else is stated.

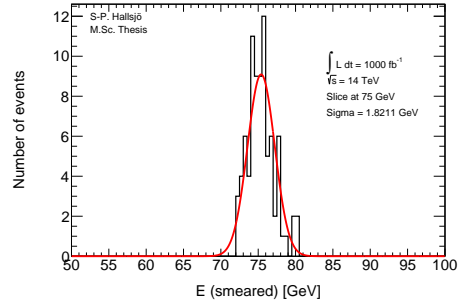
As in the comparison, figure 2.1, figure 2.2, figure 2.4 and figure 2.5 are divided depending on the different η values.

2.3.1 Electron and photon

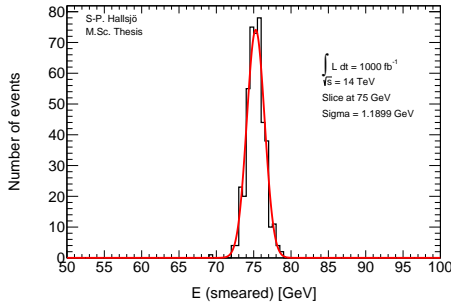
Since these are detected very similarly in the detector, their smearing functions are identical. The peak value represents at which value of unsmeared energy or momentum this smearing occurs. In figure 2.1 the Gaussian fit (red) and the data (black) are given for the electron energies.



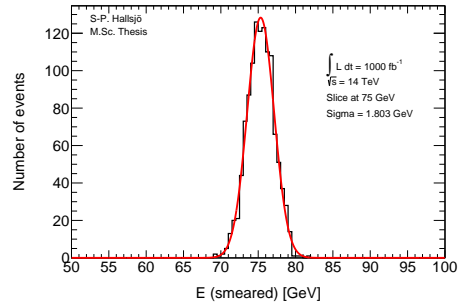
(a) Electron energy after smearing for $|\eta| < 1.4$.



(b) Electron energy after smearing for $1.4 < |\eta| < 2.47$.



(c) Photon energy after smearing for $|\eta| < 1.4$.

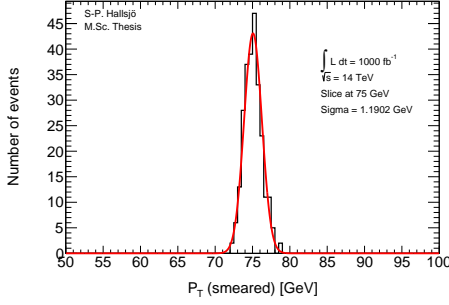


(d) Photon energy after smearing for $1.4 < |\eta| < 2.47$.

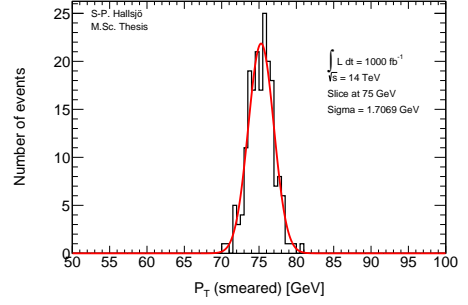
Figure 2.1: Photon and electron energy after smearing.

2.3.2 Muon

Since muons detection is shielded from the effects of pile-up only efficiency and detector limitations affect the smearing. In figure 2.2 the Gaussian fit (red) and the data (black) are given for the muon momenta.



(a) Muon momenta after smearing for $|\eta| < 1.05$.

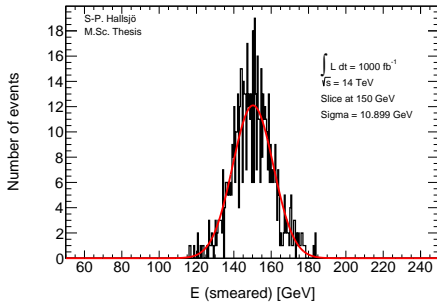


(b) Muon momenta after smearing for $1.05 < |\eta|$.

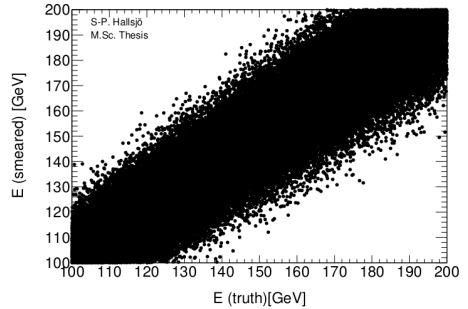
Figure 2.2: Muon momenta after smearing.

2.3.3 Tau

As described in subsection 2.1.3 taus are detected similarly to electrons and photons. Thus the plots should look similarly to those in the previous subsection apart from the peak value being at 150 GeV. In figure 2.3a the Gaussian fit (red) and the data (black) are given for tau detected through 3 prong. In figure 2.3b smeared energy is plotted against truth energy.



(a) Tau energy after smearing.

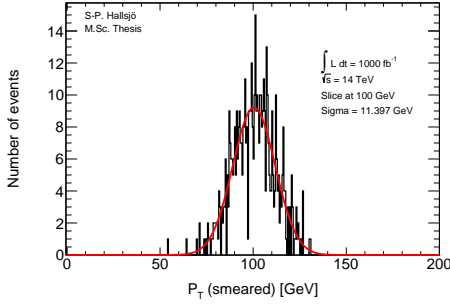


(b) Tau smeared vs truth.

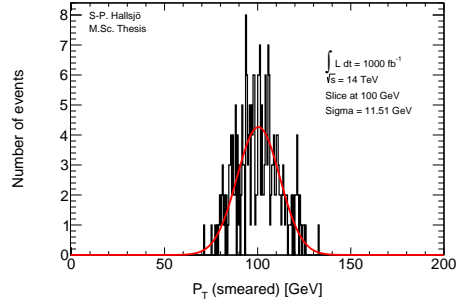
Figure 2.3: Tau energy after smearing and smeared vs truth.

2.3.4 Jets

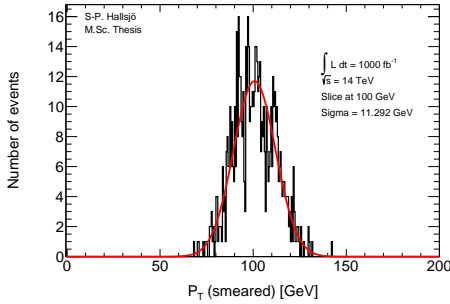
The smearing functions are divided into four different regions depending on the angle η .



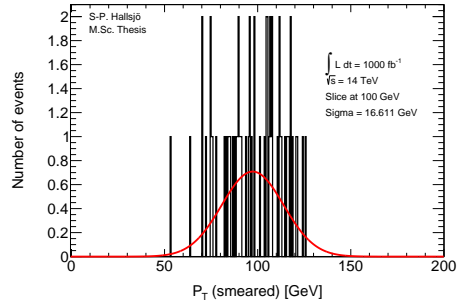
(a) Jet momenta after smearing for $|\eta| < 0.8$.



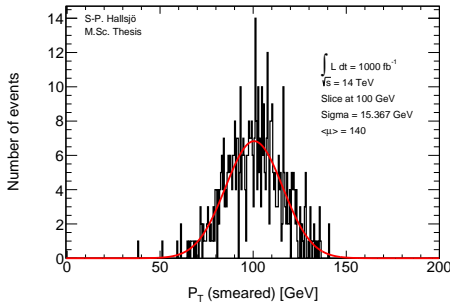
(b) For $0.8 < |\eta| < 1.2$.



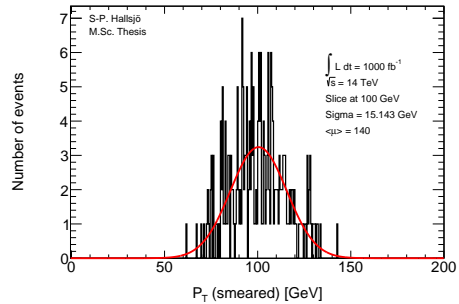
(c) Jet momenta after smearing for $1.2 < |\eta| < 2.8$.



(d) For $2.8 < |\eta| < 3.6$. Very odd due to the low amount of available data.



(e) Jet momenta after smearing for $|\eta| < 0.8$ at $\langle\mu\rangle = 140$.



(f) For $0.8 < |\eta| < 1.2$ at $\langle\mu\rangle = 140$.

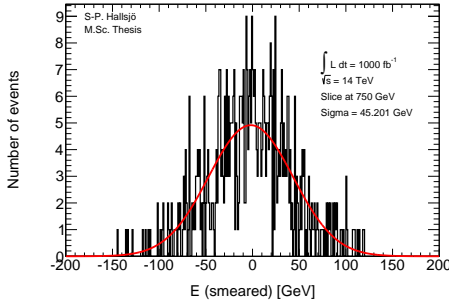
Figure 2.4: Jet momenta after smearing.

In figure 2.4 the Gaussian fit (red) and the data (black) are given for the jet momenta. Where $\langle\mu\rangle$ is the average number of simultaneous proton-proton collisions as explained in subsection 1.3.4.

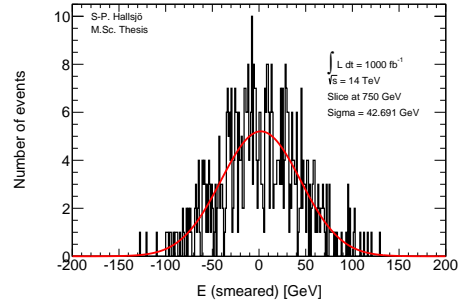
2.3.5 Missing Transversal Energy

The figures in this subsection are, compared to the above, given as absolute smearing. The central x value of 0 represents that the energy is unsmeared, compared to the others where the central x value value represents the unsmeared energy. The unsmeared energy used here is 750 GeV.

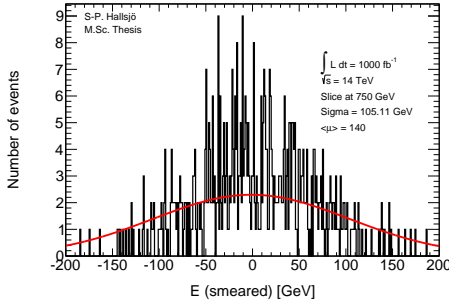
Here the E_T^{Miss} is projected down to the x- and y-axis, since these are the transverse axes, to be smeared.



(a) E_T^{Miss} smearing along the x-axis.



(b) E_T^{Miss} smearing along the y-axis.



(c) E_T^{Miss} smearing along the y-axis for $\langle\mu\rangle = 140$.

Figure 2.5: E_T^{Miss} smearing plots.

2.3.6 Summary

Since the leptons and photons are all detected by fitting detector responses to different tracks, the effect of pile-up should be that there are more track to match, but it should not affect which ones are matched. The independence of pile-up for leptons and photons is backed up in previous research, for instance [1, 32].

To validate the smearing functions, comparisons are made with [31] which gave table 2.1 for the expected resolution σ .

Process	η value	Pile-up value	σ [GeV]	Expected σ [GeV]
Electron	Low η	60	1.25 ± 0.05	1.18
	High η	60	1.82 ± 0.14	1.74
Photon	Low η	60	1.19 ± 0.04	1.18
	High η	60	1.80 ± 0.04	1.74
Muon	Low η	60	1.19 ± 0.05	1.50
	High η	60	1.71 ± 0.09	2.18
Tau	All η	60	10.9 ± 0.3	10.3
Jet	Low η	60	11.4 ± 0.4	11.6
	Low η	140	15.4 ± 0.5	15.8
	Mid low η	60	11.5 ± 0.5	11.9
	Mid low η	140	15.1 ± 0.7	15.9
	Mid high η	60	11.3 ± 0.3	10.9
	High η	60	16.6 ± 1.5	13.5
E_T^{Miss}	All η	60	43 ± 2	48
	All η	140	105 ± 12	87

Table 2.5: Calculated σ values compared to σ given from the resolution given in table 2.1. Values are given at different pile-up values for comparison.

In table 2.5 all values are given as absolute, not relative and the large difference between calculated and expected σ for Muons and E_T^{Miss} is explained by too optimistically calculated errors in σ .

2.4 Discussion

2.4.1 Dependence of smearing on pile-up

From the validation done it is interesting to note that the smearing functions were created from previous studies [1, 32] which show that detector resolution for leptons and photons is unaffected by pile-up. This may seem unexpected however it becomes quite logical when one understands how the detectors work and the effect of pile-up.

The effect of pile-up is that extra jets are introduced to the events. These jets will not reach the muon-system and thus will not affect the identification of muons. Electron, taus and photons are affected by it being harder to detect energy deposits in the calorimeter which are consistent with these particles, since there are more hits. However by restricting which deposits to consider it is possible to keep the resolution unaffected by pile-up. Jets and E_T^{Miss} will be the most affected since they rely heavily on measurements in the calorimeter and are combined of several parts, either hadronic particles or by all the transverse missing energy. Through the the formulas in table 2.1 it is seen that the effect diminishes with an increasing energy which is consistent with the description given, and that for the high energies which are of interest in this thesis the effect of pile-up is minimal.

2.4.2 Comparison to expected results

One of the major problems in the comparison was to get the significance of the Gaussian fit to be calculated correctly. The tool ROOT has a lot of different features which made this task somewhat difficult, specifically by calculating optimistic errors. A large contribution to the difficulty of calculating the significance lay in this being a statistical property and thus there is a statistical fluctuation in the result.

Another problem was to retrieve the correct resolution values from Ref. [31], since it was unclear if the resolution values given were absolute or scale dependent. This has now been corrected in a new version of the paper.

2.5 Conclusion

The smearing functions work as intended within 5.8 sigma, however when using a test box and averaging the sigmas one ends up with half of this for the extreme cases, muons and E_T^{Miss} . This indicates that the statistical fluctuation of these values and of the error calculations are considerable. Even with this statistical fluctuation the smearing functions work as intended.

3

Sensitivity to dark matter signals

The main goal of the thesis is to investigate if certain dark matter signals can be detected after the high luminosity upgrade. One immediate worry is that the background may become large in comparison to the signal, making the signal undetectable.

Another goal is to investigate if it might become more difficult to differentiate between the signal and background due to the degradation of jet and missing energy resolutions in the high luminosity upgrade.

This thesis focuses on using a luminosity of 1000 fb^{-1} and a center of mass energy of 14 TeV. The reconstructed data is created using a pile-up rate $\langle \mu \rangle = 140$ as expected during phase II.

The signal models are given in appendix A along with the background models. The two classes of models were introduced subsection 1.2.5 and will be discussed in more detail in this chapter.

Each signal model has been evaluated in different signal regions and the detectability has been evaluated using a statistical p-value.

3.1 Signal over background

3.1.1 Signal Region

An event is a recorded proton-proton collision which consists of hundreds or thousands of observables such as the number of electrons, muons, jets, tau leptons, gammas or E_T^{Miss} each with their energy and momenta.

A signal region (SR) is defined as a set of selections on event variables designed to create a sample which is enriched in signal and depleted of background. One usually tries to design the signal region so that the signal is large enough and the background small enough that one would statistically be able to either:

- Exclude the signal if the observation of the data is compatible with a background only hypothesis.
- Detect the signal and quantify the significance of the excess in data over background if the data is consistent with a signal plus background hypothesis.

How to define an optimal signal region is not known a priori and has to be studied for different signal models. The optimal region typically changes e.g with a change of the mass of new particles for instance the WIMP mass or the suppression scale. This is why there are several different signal regions studied in this thesis.

3.1.2 Cross section and luminosity weighting

Each signal or background sample is simulated at a given luminosity. These luminosities are lower than 1000fb^{-1} which is of interest in this thesis.

A weight is used to normalize different types of data so that they can be compared. As given in (1.4), the total number of events can be estimated as:

$$N = \sigma \int \mathcal{L} dt \equiv \sigma \mathcal{L}$$

Thus if the samples are generated at different luminosities the following weight should be used to rescale the samples to a new luminosity:

$$weight = \frac{\mathcal{L}\sigma}{N_{Raw}} \quad (3.1)$$

where N_{Raw} is the number simulated events for a physical, \mathcal{L} is the luminosity at which the samples are compared and σ is the cross-section.

Since each process has its own cross-section it has its own weight which is larger then one since the simulated luminosity is lower than 1000fb^{-1} . In this thesis $\mathcal{L} = 10\text{fb}^{-1}$ is used to validate the background and $\mathcal{L} = 1000\text{fb}^{-1}$ when comparing the signals to the background.

3.1.3 Background processes

To emulate the background in a proton-proton collision simulations of the main processes, which are given in table 3.1, are used.

Process
$Z \rightarrow \nu \nu$
$W \rightarrow e \nu$
$W \rightarrow \mu \nu$
$W \rightarrow \tau \nu$

Table 3.1: The main background processes from a collision. Each sample is a simulation of a physical process, the simulation names can be found in appendix A.1.

3.1.4 Verification of background normalisation

To verify that the background samples are correctly normalised they are compared with Ref. [33] in which the center of mass energy is 8 TeV and the luminosity is 10 fb^{-1} .

The cross sections at 8 TeV are about 4 times lower than cross sections at 14 TeV. These cross-sections are calculated with MadGraph[26] for the signal samples and Sherpa [27] for the background samples, as given in appendix A.

The pre-selection criteria used in Ref. [33] are the following:

- Jet veto, require no more than 2 jets with $p_T > 30 \text{ GeV}$ and $|\eta| < 4.5$. This is done to reduce the number of multi-jet events.
- Lepton veto, no electron or muon. These vetos are there to remove uninteresting $W \rightarrow e \nu$ and $W \rightarrow \mu \nu$ background events.
- Leading jet with $|\eta| < 2.0$ and $\Delta\varphi(\text{jet}, E_T^{\text{Miss}}) > 0.5$ (second-leading jet). This is done to further reduce the number of multi-jet events.

The following signal regions were used:

signal region	SR3p	SR4p
minimum leading jet p_T (GeV)	350	500
minimum E_T^{Miss} (GeV)	350	500

Table 3.2: The signal regions from Ref. [33].

The article in Ref. [33] has four signal regions in total, unfortunately since the simulated background used in this thesis is filtered before the analysis only the two highest regions are comparable. This can be seen in table 3.4 in subsection 3.3.1.

The background is compared to Ref. [33] altering the cross-sections of the samples used in this thesis to simulate a center of mass energy of 8 TeV instead of 14. This could unfortunately not be done for the signals as that would require new samples to be produced. As seen in table 3.4 and somewhat discussed in subsection 3.3.1 the events corresponded quite nicely to the values from the paper. The discrepancies are explained by general differences between simulations and measured events, such as:

- The difference in $W \rightarrow \tau \nu$ can be explained by the fact that τ can not be recreated as a jet in the simulated events which it can in measured events.
- The difference in $W \rightarrow \mu \nu$ is explained through the simulated events having a better separation of muons neutrinos and E_T^{Miss} .

3.1.5 Errors in background

To make a thorough analysis of the background it is important to take into consideration different errors that exist in the predicted number of events. This is especially important when looking at which signals can be excluded in different signal regions since a large uncertainty on the background has a negative impact on the sensitivity to the signal.

The uncertainties are divided into three categories:

- Uncertainty due to limited Monte Carlo (MC) statistics.
The statistical errors from MC come from the number of events that are generated for a certain process and can not be estimated since it is not known how many events which will be simulated in the future.
- Uncertainty due to limited statistics in data control regions.
A control region (CR) is the opposite to a signal region, criteria set so that there is a region with almost no signal. In this CR there will still be fluctuations in the amount of background events due to statistical effects, which can then be measured. The numerical value, whose size is a priori constant with the luminosity, has been take from Ref. [33] as $\frac{30}{380}$ and is assumed to decrease with the increased luminosity as $\frac{1}{\sqrt{L}}$.
- Other systematic errors.
The systematic errors are fixed errors which are always present coming from different approximations in how all the events are generated. The other systematic errors have been given two different values, from Ref. [33] as $\frac{30}{380}$ or 0.02.

Using the errors above results in two different models of the total error in the background σ_B which is defined as:

$$\sigma_B = \text{Statistical error from MC} \oplus \text{Statistical error in CR} \oplus \text{Other errors}$$

Numerically the total error being used is 0.08 or 0.02.

3.1.6 Figure of merit

To be able to evaluate different signal regions and different signal models, a figure of merit p is used. The value p is the probability for the observed background to fluctuate to the value of the signal plus background. Thus if the p -value is small it is improbable that the observed background could result in the same value as if there is a signal and background. This means that for a sufficiently small p -value the signal is detectable. The limiting value in this thesis is taken as $p=0.05$, everything under is considered detectable.

Assuming the expected number of background events are $B \pm \sigma_B$ where σ_B is the quadratic sum of the errors as explained in subsection 3.1.5. The expected number of signal events is S , assumed without fluctuation.

If no uncertainty in B or S is assumed, then the probability that the background will fluctuate up to the signal and background should follow a Poisson distribution as such:

$$P(S+B|B) = \frac{e^{-B} B^{(S+B)}}{(S+B)!} \quad (3.2)$$

The probability that the observed number of background events O will fluctuate to a value larger or equal to the signal plus background then becomes:

$$P(O \geq S+B|B) = \sum_{k=S+B}^{\infty} \frac{e^{-B} B^k}{k!} \quad (3.3)$$

However since there is an uncertainty in the background, the probability distribution $P(O \geq S+B|B)$ must be weighted with a Gaussian function:

$$G(N_B|B, \sigma_B) = \frac{1}{\sigma_B \sqrt{2\pi}} e^{-\frac{(O-B)^2}{2\sigma_B^2}} \quad (3.4)$$

where N_B is the expected number of background events.

The probability of the background fluctuating to signal plus background is calculated as:

$$p = \int_{-\infty}^{\infty} P(O \geq S+B|N_B) G(N_B|B, \sigma_B) dN_B \quad (3.5)$$

3.1.7 D5 operator models

As described in subsection 1.2.5, one of the signals is modelled using the D5 operator. In this thesis two different scenarios are used, one at a dark matter mass of 50 GeV and one at 400 GeV. The different datasets for the signals are presented in table A.3 in appendix A.2.2.

Each of these models are modelled with a mass suppression scale, denoted M^* , at 10000 GeV which is connected to the cross-section as shown in (3.6). To study

another M^* the cross section has to be altered by using (3.6).

$$\sigma(M^*) = \frac{\sigma_{reference}}{M^*} \quad (3.6)$$

where $\sigma_{reference}$ is the theoretically calculated sigma. In subsection 3.3.3 it is determined which values of M^* can be excluded with the upgraded LHC phase 2 upgrade and ATLAS.

3.1.8 Light vector mediator models

As described in subsection 1.2.5, the other signal model is a vector mediator model. In this thesis these signals have two different width scenarios, $M/3$ and $M/8\pi$ where M denotes the mediator mass. The width scenarios contain eight different mediator mass scenarios with masses between 100 and 15000 GeV. In addition to this there are, as with the D5 operator, two different dark matter masses, one at 50 GeV and one at 400 GeV. The different datasets are presented in table A.4 in appendix A.2.3.

The models found to be excludable are presented in subsection 3.3.4.

3.2 Signal regions

3.2.1 Signal region definitions

To be able to compare signal results to previous studies new signal regions were devised. When simulated only 2 % of the estimated signal events passed the pre-selection criteria compared to estimations. Thus these new pre-selection criteria were devised to increase the amount of signal.

The following pre-selection criteria are used:

- Jet veto, require no more than 2 jets with $p_T > 30\text{GeV}$ and $|\eta| < 4.5$. This is done to reduce the number of multi-jet events.
- Electron veto which is defined: $\Delta R(jet^{lead}, electron^{lead}) \geq 0.4$ and $electron^{lead} p_T > 20\text{GeV}$ removed.
- Muon veto which is defined: $\Delta R(jet^{lead}, muon^{lead}) \geq 0.4$ and $muon^{lead} p_T > 20\text{GeV}$ removed. These formulation of vetos are used to remove uninteresting $W \rightarrow e\nu$ and $W \rightarrow \mu\nu$ background events with out removing to much of the signal. The ΔR involvement is to make sure the veto is only on simulated true particles and not simulated false detections.
- Leading jet with $|\eta| < 2.0$ and $\Delta\phi(jet, E_T^{Miss}) > 0.5$ (second-leading jet). This is done to further reduce the number of multi-jet events.

where the superscript lead denotes the the entity with highest transverse momentum p_T . Thus $electron^{lead}$ would be the simulated electron in an event with the highest p_T .

To try and minimize the amount of background compared to the amount of signal following signal regions are used:

Symmetric signal region	SR1	SR1p	SR2	SR3	SR4
minimum leading jet p_T (GeV)	350	500	600	800	1000
minimum E_T^{Miss} (GeV)	350	500	600	800	1000
Asymmetric signal region	SRa	SRb	SRc	SRd	
minimum leading jet p_T (GeV)	350	350	350	350	
minimum E_T^{Miss} (GeV)	350	600	800	1000	

Table 3.3: The new signal regions.

These are constructed to be similar to previous studies and by looking at the distribution of leading jet p_T and E_T^{Miss} for the signal and background samples.

3.2.2 Verifying background data

The choice of a new electron and muon veto require the comparison from subsection 3.1.4 to be redone. As seen in table 3.5 the events corresponded quite nicely to the values from the paper and are somewhat better than the previous comparison which can be seen in subsection 3.3.1.

3.3 Results

3.3.1 Verifying background data

In table 3.4 and table 3.5 a comparison is shown between the number of events in this work using 8 TeV center of mass energy cross section for 1000 fb^{-1} at a truth level and the number of expected events predicted in Ref. [33] scaled to 1000 fb^{-1} . Truth data was used to not let the increased pile-up value affect the comparison. It can be seen that the simulated events and expected events coincide well for all processes and all regions apart from $W \rightarrow \tau \nu$, $W \rightarrow \mu \nu$ and thus the total as well.

Process	SR3p		SR4p	
	Simulated	From paper	Simulated	From paper
$Z \rightarrow \nu \nu$	140298	152000	25250	27000
$W \rightarrow \tau \nu$	40701	37000	5862	3900
$W \rightarrow e \nu$	11229	11200	1507	1600
$W \rightarrow \mu \nu$	13727	15800	1872	4200
Total background	205955	218000	34491	36700

Table 3.4: Comparison of the simulated and expected events from Ref. [33] at $\mathcal{L} = 1000 \text{ fb}^{-1}$, cross-sections corresponding to $\sqrt{s} = 8 \text{ TeV}$.

Process	SR1		SR1p	
	Simulated	From paper	Simulated	From paper
$Z \rightarrow \nu \nu$	150753	152000	27569	27000
$W \rightarrow \tau \nu$	49320	37000	7318	3900
$W \rightarrow e \nu$	18329	11200	2534	1600
$W \rightarrow \mu \nu$	22290	15800	3218	4200
Total background	240690	218000	40639	36700

Table 3.5: Comparison of the simulated and expected events from Ref. [33] with $\mathcal{L} = 1000 \text{ fb}^{-1}$, cross-sections corresponding to $\sqrt{s} = 8 \text{ TeV}$ and using a modified electron and muon veto as discussed in subsection 3.2.1.

3.3.2 Signal and background events in signal regions

In the following tables the number of events are given using one of the D5 operators as the signal, and the background in the different signal regions at $\sqrt{s} = 14 \text{ TeV}$ and $\mathcal{L} = 1000 \text{ fb}^{-1}$. The number of background events is used to calculate exclusion limits on M^* and on the mediator mass models.

Process	SR1	SR2	SR3	SR4	SRa	SRb	SRc	SRd
D5, $m_\chi = 50$ GeV, $M^*=1$ TeV	131844	30900	11053	4532	131844	37217	13280	5387
$Z \rightarrow \nu\nu$	619752	44146	8764	2205	619752	61193	11975	2998
$W \rightarrow \tau\nu$	169983	8753	1479	344	169983	12047	2032	453
$W \rightarrow e\nu$	63026	2986	510	114	63026	4114	688	160
$W \rightarrow \mu\nu$	76618	3880	658	162	76618	5094	871	199
Total background	929379	59765	11411	2825	929379	82448	15566	3810

Table 3.6: Signal and background events for truth data in the signal regions at $\sqrt{s} = 14$ TeV and $\mathcal{L} = 1000\text{fb}^{-1}$.

Process at $\sqrt{s} = 14\text{TeV}$	SR1	SR2	SR3	SR4	SRa	SRb	SRc	SRd
D5, $m_\chi = 50$ GeV, $M^*=1$ TeV	122117	28663	10273	4259	122117	39618	14151	5679
$Z \rightarrow \nu\nu$	568410	40518	8012	2023	568410	74564	13817	3318
$W \rightarrow \tau\nu$	170999	8644	1442	314	170999	16241	2446	536
$W \rightarrow e\nu$	60071	2799	470	110	60071	5366	835	183
$W \rightarrow \mu\nu$	73495	3704	629	152	73495	6622	1046	236
Total background	872975	55665	10552	2599	872975	102793	18144	4273

Table 3.7: Signal and background events for reconstructed data with $\langle\mu\rangle = 140$ in the signal regions at $\sqrt{s} = 14$ TeV and $\mathcal{L} = 1000\text{fb}^{-1}$.

Table 3.6 and table 3.7 show how the ratio between the number of signal events and total background increases from the first (SR1/SRa) to the last signal region (SR4/SRd) which illustrates that these are good choices of signal regions. The difference between SR4 and SRd show clearly the effect of the lead jet momenta cut. Comparing the two tables it is interesting to see that they are similar even though table 3.7 is reconstructed with a pile-up rate of 140 which is consistent with a small effect of pile-up.

3.3.3 Project exclusion limits on M^*

For the D5 operators as described in subsection 3.1.7 limits on the mass suppression scale has been calculated by calculating the p-value for each value of M^* in the range 0 to 2500 GeV and finding which values of M^* lead to $p < 0.05$. This is done using the two different error models as described in subsection 3.1.6 as figures of merit.

The limit is found, seen as a horizontal line in both figure 3.1 and figure 3.2, when the p-value = 0.05. In these figures the effect of the error model can be seen as a left shift but no change in incline. The p-value is low at low M^* since the cross-section is large which lead to a large signal which is easy to exclude. Higher values of M^* decrease the value of the cross-section making it more difficult and finally improbable to distinguish the signal from the background. For example a p-value of 0.5 indicated that the observed value of the background has a 50 % chance to fluctuate to the value of signal plus background.

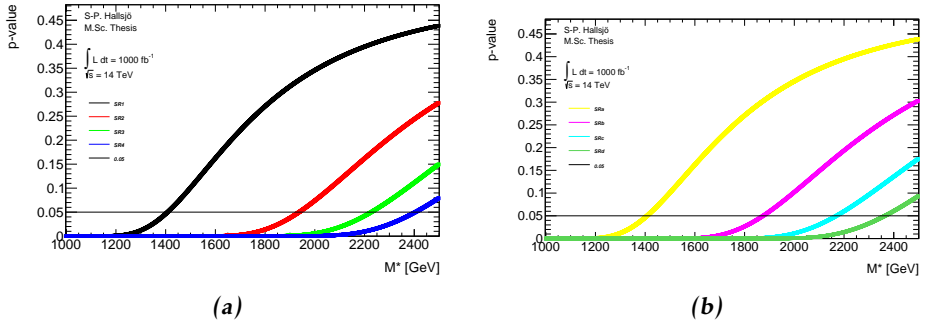


Figure 3.1: p-value as a function of the mass suppression scale M^* at truth level for error model 0.02.

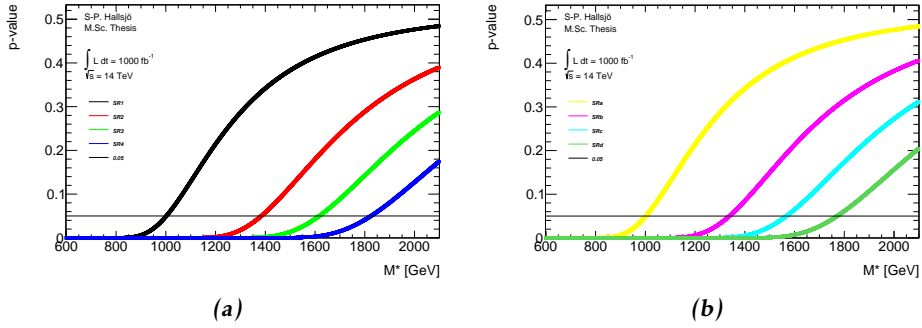


Figure 3.2: p -value as a function of the mass suppression scale M^* at truth level for error model 0.08.

Calculating the intersection between these lines and 0.05 results in tables 3.8-3.11 for both a dark matter mass of 50 GeV and at 400 GeV with the different error models.

Signal region	Truth [GeV]	Reconstructed [GeV]
SR1, symmetric 350 GeV	1407	1402
SR2, symmetric 600 GeV	1936	1934
SR3, symmetric 800 GeV	2227	2226
SR4, symmetric 1000 GeV	2404	2406
SRa, symmetric 350 GeV	1425	1421
SRb, asymmetric 600 GeV	1874	1803
SRc, asymmetric 800 GeV	2169	2125
SRd, asymmetric 1000 GeV	2365	2340

Table 3.8: Limits on mass suppression scales in GeV given for $m_\chi = 50$ GeV and the 0.02 error model.

Signal region	Truth [GeV]	Reconstructed [GeV]
SR1, symmetric 350 GeV	1002	999
SR2, symmetric 600 GeV	1384	1382
SR3, symmetric 800 GeV	1617	1619
SR4, symmetric 1000 GeV	1825	1834
SRa, symmetric 350 GeV	1338	1286
SRb, asymmetric 600 GeV	1356	1303
SRc, asymmetric 800 GeV	1567	1533
SRd, asymmetric 1000 GeV	1771	1745

Table 3.9: Limits on mass suppression scales in GeV given for $m_\chi = 50$ GeV and the 0.08 error model.

Signal region	Truth [GeV]	Reconstructed [GeV]
SR1, symmetric 350 GeV	1333	1329
SR2, symmetric 600 GeV	18481	1847
SR3, symmetric 800 GeV	2162	2163
SR4, symmetric 1000 GeV	2332	2303
SRa, symmetric 350 GeV	1350	1346
SRb, asymmetric 600 GeV	1789	1721
SRc, asymmetric 800 GeV	2106	2059
SRd, asymmetric 1000 GeV	2288	2258

Table 3.10: Limits on mass suppression scales in GeV given for $m_\chi = 400$ GeV and the 0.02 error model.

Signal region	Truth [GeV]	Reconstructed [GeV]
SR1, symmetric 350 GeV	949	946
SR2, symmetric 600 GeV	1321	1320
SR3, symmetric 800 GeV	1570	1573
SR4, symmetric 1000 GeV	1770	1755
SRa, symmetric 350 GeV	961	959
SRb, asymmetric 600 GeV	1277	1228
SRc, asymmetric 800 GeV	1521	1484
SRd, asymmetric 1000 GeV	1714	1684

Table 3.11: Limits on mass suppression scales in GeV given for $m_\chi = 400$ GeV and the 0.08 error model.

Tables 3.8-3.11 show the significant difference between the different signals regions, especially between SR4 and SRd which are similar apart from the lead jet momenta cut. Another interesting difference is how the limits are increased by using tighter signal regions. In these tables the effect from an increase in dark matter mass can be seen as small.

The effect of pile-up on M^* can be seen by compensating the columns. The limits at reconstructed level can be better than at truth since the statistical approach by the smearing functions can either increase or decrease the number of events which are in a signal region. If the number of signal events is increased and the number of background events decreased the M^* values will increase.

3.3.4 Projection exclusion limits on mediator mass models

For the vector mediator modes described in subsection 3.1.8 limits on which models can be excluded have been calculated. This is done by calculating which models have a p-value below 0.05. An example of an excludable and an unexcludable signal model can be seen in figure 3.3. The exclusion uses the two different error models, as described in subsection 3.1.6, when calculating the p-value. All signals which have been used can be found in appendix A.2.3.

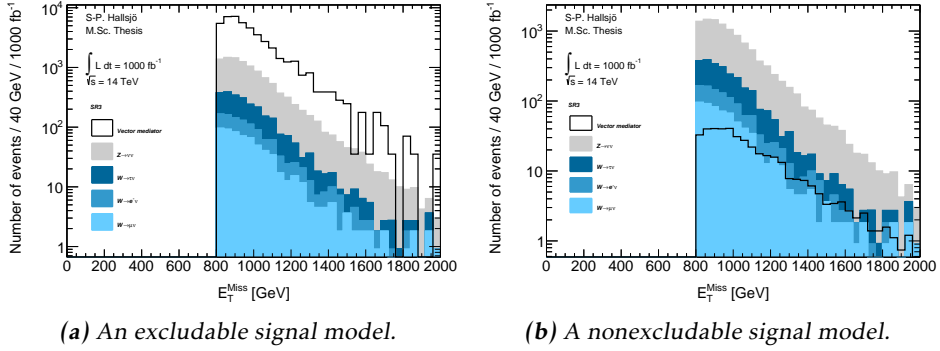


Figure 3.3: Signal on background plot in log-scale for E_T^{Miss} on a reconstructed level in SR3 to illustrate a signal which is excludable and one which is not.

To set limits on the mediator mass models the p-value is calculated in different signal regions for the different signal models with different mediator mass. As an example a plot of this in signal region d is given in figure 3.4 where the p-value of the models is plotted against the increasing mediator mass for different widths and dark matter masses. The result of which models are excludable, thus with a p-value < 0.05 are given in tables 3.12 and 3.13.

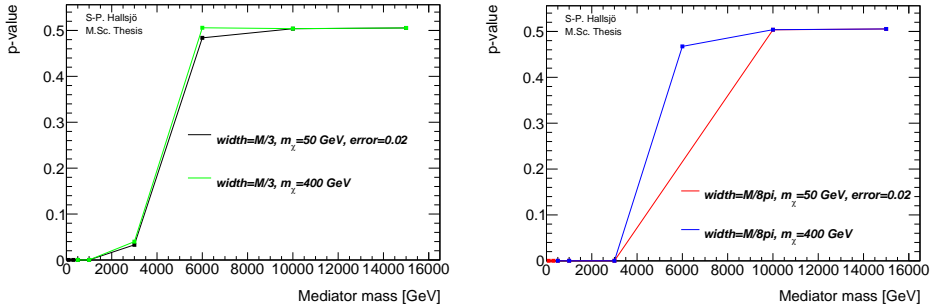


Figure 3.4: P-values at a reconstructed level for the the different mediator masses, dark matter masses and different widths which were investigated in SRd.

What can be seen in table 3.12 and table 3.13 is that the models are robust since the limits are unchanged by a change in the error models and with the intro-

width	$m_\chi = 50$ GeV	$m_\chi = 400$ GeV
M/3	1000 GeV	1000 GeV
M/8pi	3000 GeV	3000 GeV

Table 3.12: Limits on the highest mediator mass model which can be excluded for different widths, different dark matter masses for truth and re-constructed data and both error models in SR2, 3, 4, c, d.

width	$m_\chi = 50$ GeV	$m_\chi = 400$ GeV
M/3	1000 GeV	1000 GeV
M/8pi	1000 GeV	1000 GeV

Table 3.13: Limits on the highest mediator mass model which can be excluded for different widths, different dark matter masses for truth and re-constructed data and both error models in SRb.

duction of pile-up. However since there were no signal models available with mediator masses between 1000 and 3000 or between 3000 and 6000 noting can really be said. These effects may be more visible when determining the mediator mass limit similar to the work done for M^* and will also set the limits on the mediator mass.

It is though quite interesting to see that SRb compared to the other signal regions, is the signal region which was worst suited for the vector mediator signals. By looking at the definition of this signal region would suggest that the background is less susceptible to a lead jet cut than the signals.

3.4 Discussion

3.4.1 Comparison to previous results

In table 3.14 the limits for the mass suppression scale are given from both the paper and from this work. It is seen that the increase in luminosity and center of mass energy gives an increase of the mass suppression scale by a factor of 2-3.

Dark matter mass	From simulation	From paper
50 GeV	1960 GeV	800 GeV
400 GeV	1871 GeV	700 GeV

Table 3.14: M^* values in SR2 from both simulation at 14 TeV, 1000fb^{-1} and from Ref. [33] at 8 TeV and 10fb^{-1} .

3.4.2 Effect of the high luminosity

As seen in section 3.3, the effect of a pile-up rate of 140 is minute in the signal regions chosen. The primary focus of this thesis was to look at the effect of pile-up, and try to mitigate the effect of it. However it is shown here that by choosing signal regions with a high enough requirement the effect is minute. Thus the focus was shifted to perform a more in-depth mono-jet analysis of different dark matter signal models.

For the mass suppression scale, as seen in subsection 3.3.3, comparing the truth values against the reconstructed values the difference is at most $< 5\%$. Thus these signal regions are preferable for use in the high luminosity upgrade.

Regarding the mediator models, as discussed in subsection 3.3.4 the models are sensitive to exclusion regardless of truth or reconstructed data. By investigating more models the limits can on the mediator masses can be set and the effects of pile-up seen more clearly.

3.5 Conclusion

3.5.1 Limit on M^*

The limits can be found in subsection 3.3.3 and are 2-3 times better than previous results at 8 TeV and 10fb^{-1} .

3.5.2 Limit on mediator mass models

The limits are found in subsection 3.3.4 and is the first result done with these models and thus can not be compared.

3.5.3 Effect of the high luminosity

At a pile-up level of 140 the effect is at most $< 5\%$ compared to truth level on the mass suppression scale and does not affect the vector mediator models which are robust as discussed in subsection 3.4.2.

4

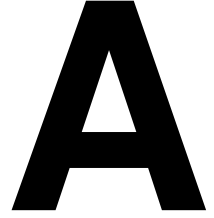
Final remarks

In this thesis an introduction is given to phenomena in elementary particle physics, see chapter 1. After this a validation of smearing functions is done to validate that the measured resolution is compatible with what is expected, see chapter 2. In this chapter, table 2.1 contains the expected resolutions. Finally in chapter 3 two different dark matter signal models are investigated, both an effective theory and a vector mediator model.

The suggestions for future research come from what would have been done if time was not an issue. With an unlimited amount of time chapter 3 would have been expanded to contain several different effective theory models and consider models which are based on Supersymmetry. Another interesting continuation would be to investigate new signal regions to see if it is possible to mitigate the effects of high luminosity even at low energies. This may be possible by using other selection criteria. Similarly it would be interesting to see if there are better selection criteria to increase the ratio of signal to background.

The most interesting continuation of this work would be to compare the results given here to measurements done after the phase II upgrade, and hopefully see characteristic signatures from WIMPS.

Appendix



Datasets

A.1 Background processes

All datasets used are d4pd which is a data format used at CERN.

A.1.1 Validation

For the validation the following datasets were used.

ATLAS dataset	Process	Generator	Boson p_T cut [GeV]
157539	$Z \rightarrow \nu\nu$	SHERPA	450
157534	$W \rightarrow e\nu$	SHERPA	450
157535	$W \rightarrow \tau\nu$	SHERPA	450
157536	$W \rightarrow \tau\nu$	SHERPA	450
129160	Jet sample	PYTHIA8	450
129170	γ + jet sample	PYTHIA8	450

Table A.1: Validation samples used. Boson cut indicates a cut on lead jet and E_T^{Miss} .

A.1.2 Background for signals

ATLAS dataset	Process	Generator	Boson p_T cut [GeV]	Cross-section [pb]
157539	$Z \rightarrow \nu\nu$	SHERPA	280	5.67
157534	$W \rightarrow e\nu$	SHERPA	200	27.77
157535	$W \rightarrow \tau\nu$	SHERPA	200	27.74
157536	$W \rightarrow \tau\nu$	SHERPA	200	27.74

Table A.2: Background samples used. Boson cut indicates a cut on lead jet and E_T^{Miss} . The cross-sections are given at $\sqrt{s} = 14$ TeV.

A.2 Signals

A.2.1 Q_{cut}

Q_{cut} means that the original data has been split into different intervals depending on the value of the lead jet momenta. Each of the different contributions need to be summed to get the full signal.

A.2.2 D5 signal processes

ATLAS dataset	Generator	m_χ [GeV]	M^* [GeV]	Q_{cut} [GeV]	Cross-section [pb]
188408	MADGRAPH+PHYTHIA	50	10000	200	$4.34 \cdot 10^{-5}$
188409	MADGRAPH+PHYTHIA	50	10000	400	$1.09 \cdot 10^{-5}$
188410	MADGRAPH+PHYTHIA	50	10000	600	$5.61 \cdot 10^{-6}$
188411	MADGRAPH+PHYTHIA	400	10000	200	$3.42 \cdot 10^{-5}$
188412	MADGRAPH+PHYTHIA	400	10000	400	$8.51 \cdot 10^{-6}$
188413	MADGRAPH+PHYTHIA	400	10000	600	$4.70 \cdot 10^{-6}$

Table A.3: Datasets based on the D5-operator.

A.2.3 Light vector mediator processes

ATLAS dataset	Generator	m_χ [GeV]	Mediator mass [GeV]	Width [GeV]	Q_{cut} [GeV]	Cross-section [pb]
188414	MADGRAPH+PHYTHIA	50	100	M/3	200	33.80
188422	MADGRAPH+PHYTHIA	50	100	M/3	400	2.86
188430	MADGRAPH+PHYTHIA	50	100	M/3	600	0.70
188415	MADGRAPH+PHYTHIA	50	300	M/3	200	17.40
188423	MADGRAPH+PHYTHIA	50	300	M/3	400	2.00
188431	MADGRAPH+PHYTHIA	50	300	M/3	600	0.53
188416	MADGRAPH+PHYTHIA	50	500	M/3	200	8.09
188424	MADGRAPH+PHYTHIA	50	500	M/3	400	0.95
188432	MADGRAPH+PHYTHIA	50	500	M/3	600	0.30
188417	MADGRAPH+PHYTHIA	50	1000	M/3	200	0.99
188425	MADGRAPH+PHYTHIA	50	1000	M/3	400	0.20
188433	MADGRAPH+PHYTHIA	50	1000	M/3	600	$8.56 \cdot 10^{-2}$
188418	MADGRAPH+PHYTHIA	50	3000	M/3	200	$1.30 \cdot 10^{-2}$
188426	MADGRAPH+PHYTHIA	50	3000	M/3	400	$3.21 \cdot 10^{-3}$
188434	MADGRAPH+PHYTHIA	50	3000	M/3	600	$1.85 \cdot 10^{-3}$
188419	MADGRAPH+PHYTHIA	50	6000	M/3	200	$4.31 \cdot 10^{-4}$
188427	MADGRAPH+PHYTHIA	50	6000	M/3	400	$1.01 \cdot 10^{-4}$
188435	MADGRAPH+PHYTHIA	50	6000	M/3	600	$5.46 \cdot 10^{-5}$
188420	MADGRAPH+PHYTHIA	50	10000	M/3	200	$4.82 \cdot 10^{-5}$
188428	MADGRAPH+PHYTHIA	50	10000	M/3	400	$1.08 \cdot 10^{-5}$
188436	MADGRAPH+PHYTHIA	50	10000	M/3	600	$5.55 \cdot 10^{-6}$
188421	MADGRAPH+PHYTHIA	50	15000	M/3	200	$9.07 \cdot 10^{-6}$
188429	MADGRAPH+PHYTHIA	50	15000	M/3	400	$2.02 \cdot 10^{-6}$
188437	MADGRAPH+PHYTHIA	50	15000	M/3	600	$1.04 \cdot 10^{-6}$
188438	MADGRAPH+PHYTHIA	50	100	M/8pi	200	115.55
188446	MADGRAPH+PHYTHIA	50	100	M/8pi	400	9.17
188454	MADGRAPH+PHYTHIA	50	100	M/8pi	600	2.23
188439	MADGRAPH+PHYTHIA	50	300	M/8pi	200	168.40
188447	MADGRAPH+PHYTHIA	50	300	M/8pi	400	18.46

188455	MADGRAPH+PHYTHIA	50	300	M/8pi	600	4.66
188440	MADGRAPH+PHYTHIA	50	500	M/8pi	200	64.12
188448	MADGRAPH+PHYTHIA	50	500	M/8pi	400	9.30
188456	MADGRAPH+PHYTHIA	50	500	M/8pi	600	2.84
188441	MADGRAPH+PHYTHIA	50	1000	M/8pi	200	9.43
188449	MADGRAPH+PHYTHIA	50	1000	M/8pi	400	2.02
188457	MADGRAPH+PHYTHIA	50	1000	M/8pi	600	0.87
188442	MADGRAPH+PHYTHIA	50	3000	M/8pi	200	$8.21 \cdot 10^{-2}$
188450	MADGRAPH+PHYTHIA	50	3000	M/8pi	400	$2.25 \cdot 10^{-2}$
188458	MADGRAPH+PHYTHIA	50	3000	M/8pi	600	$1.41 \cdot 10^{-2}$
188444	MADGRAPH+PHYTHIA	50	10000	M/8pi	200	$5.30 \cdot 10^{-5}$
188452	MADGRAPH+PHYTHIA	50	10000	M/8pi	400	$1.20 \cdot 10^{-5}$
188460	MADGRAPH+PHYTHIA	50	10000	M/8pi	600	$6.22 \cdot 10^{-6}$
188445	MADGRAPH+PHYTHIA	50	15000	M/8pi	200	$1.01 \cdot 10^{-5}$
188453	MADGRAPH+PHYTHIA	50	15000	M/8pi	400	$2.24 \cdot 10^{-6}$
188461	MADGRAPH+PHYTHIA	50	15000	M/8pi	600	$1.16 \cdot 10^{-6}$
188462	MADGRAPH+PHYTHIA	400	500	M/3	200	0.20
188468	MADGRAPH+PHYTHIA	400	500	M/3	400	$3.84 \cdot 10^{-2}$
188474	MADGRAPH+PHYTHIA	400	500	M/3	600	$1.71 \cdot 10^{-2}$
188463	MADGRAPH+PHYTHIA	400	1000	M/3	200	0.59
188469	MADGRAPH+PHYTHIA	400	1000	M/3	400	0.13
188475	MADGRAPH+PHYTHIA	400	1000	M/3	600	$5.80 \cdot 10^{-2}$
188464	MADGRAPH+PHYTHIA	400	3000	M/3	200	$1.12 \cdot 10^{-2}$
188470	MADGRAPH+PHYTHIA	400	3000	M/3	400	$2.92 \cdot 10^{-3}$
188476	MADGRAPH+PHYTHIA	400	3000	M/3	600	$1.74 \cdot 10^{-3}$
188465	MADGRAPH+PHYTHIA	400	6000	M/3	200	$3.29 \cdot 10^{-4}$
188471	MADGRAPH+PHYTHIA	400	6000	M/3	400	$8.35 \cdot 10^{-5}$
188477	MADGRAPH+PHYTHIA	400	6000	M/3	600	$5.81 \cdot 10^{-5}$
188466	MADGRAPH+PHYTHIA	400	10000	M/3	200	$3.43 \cdot 10^{-5}$
188472	MADGRAPH+PHYTHIA	400	10000	M/3	400	$8.50 \cdot 10^{-6}$
188478	MADGRAPH+PHYTHIA	400	10000	M/3	600	$4.76 \cdot 10^{-6}$

188467	MADGRAPH+PHYTHIA	400	15000	M/3	200	$6.41 \cdot 10^{-6}$
188473	MADGRAPH+PHYTHIA	400	15000	M/3	400	$1.58 \cdot 10^{-6}$
188479	MADGRAPH+PHYTHIA	400	15000	M/3	600	$8.80 \cdot 10^{-7}$
188480	MADGRAPH+PHYTHIA	400	500	M/8pi	200	0.18
188486	MADGRAPH+PHYTHIA	400	500	M/8pi	400	$3.87 \cdot 10^{-2}$
188492	MADGRAPH+PHYTHIA	400	500	M/8pi	600	$1.72 \cdot 10^{-2}$
188481	MADGRAPH+PHYTHIA	400	1000	M/8pi	200	7.23
188487	MADGRAPH+PHYTHIA	400	1000	M/8pi	400	1.54
188493	MADGRAPH+PHYTHIA	400	1000	M/8pi	600	0.67
188482	MADGRAPH+PHYTHIA	400	3000	M/8pi	200	$8.05 \cdot 10^{-2}$
188488	MADGRAPH+PHYTHIA	400	3000	M/8pi	400	$2.20 \cdot 10^{-2}$
188494	MADGRAPH+PHYTHIA	400	3000	M/8pi	600	$1.39 \cdot 10^{-2}$
188483	MADGRAPH+PHYTHIA	400	6000	M/8pi	200	$5.48 \cdot 10^{-4}$
188489	MADGRAPH+PHYTHIA	400	6000	M/8pi	400	$1.44 \cdot 10^{-4}$
188495	MADGRAPH+PHYTHIA	400	6000	M/8pi	600	$8.68 \cdot 10^{-5}$
188484	MADGRAPH+PHYTHIA	400	10000	M/8pi	200	$3.80 \cdot 10^{-5}$
188490	MADGRAPH+PHYTHIA	400	10000	M/8pi	400	$9.54 \cdot 10^{-6}$
188496	MADGRAPH+PHYTHIA	400	10000	M/8pi	600	$5.35 \cdot 10^{-6}$
188485	MADGRAPH+PHYTHIA	400	15000	M/8pi	200	$7.17 \cdot 10^{-6}$
188491	MADGRAPH+PHYTHIA	400	15000	M/8pi	400	$1.78 \cdot 10^{-6}$
188497	MADGRAPH+PHYTHIA	400	15000	M/8pi	600	$9.78 \cdot 10^{-7}$

Table A.4: Datasets based on the light vector mediator model.

Bibliography

- [1] Collaboration ATLAS. Letter of Intent for the Phase-II Upgrade of the ATLAS Experiment. Dec 2012. URL <https://cds.cern.ch/record/1502664/>. Cited on pages 1, 9, 17, 28, and 29.
- [2] B.H. Bransden and C.J. Joachain. *Quantum mechanics*. Pearson Education, second edition, 2000. Cited on page 3.
- [3] S-P. Hallsjö. Covering the sphere with noncontextuality inequalities. Bachelor's thesis, Linköping University, The Institute of Technology, 2013. URL <http://urn.kb.se/resolve?urn=urn:nbn:se:liu:diva-103663>. Cited on page 3.
- [4] A. Zee. *Quantum Field Theory in a Nutshell*. Princeton University Press, illustrated edition, March 2003. ISBN 0691010196. Cited on pages 3, 4, and 7.
- [5] H. Goldstein, C. P. Poole, and J. L. Safko. *Classical Mechanics (3rd Edition)*. Addison-Wesley, 3 edition, June 2001. ISBN 0201657023. Cited on page 3.
- [6] W. Herr and B. Muratori. Concept of luminosity. 2006. URL <http://cds.cern.ch/record/941318/>. Cited on pages 3 and 4.
- [7] W. E. Burcham and M. Jobes. *Nuclear and Particle Physics*. Pearson education, second edition, 1995. Cited on page 4.
- [8] The ATLAS Collaboration. Observation of a new particle in the search for the Standard Model Higgs boson with the ATLAS detector at the LHC. *Phys. Lett. B*, 716 (arXiv:1207.7214. CERN-PH-EP-2012-218):1–29. 39 p, Aug 2012. Cited on page 4.
- [9] Serguei Chatrchyan et al. Observation of a new boson at a mass of 125 GeV with the CMS experiment at the LHC. *Phys.Lett.*, B716:30–61, 2012. doi: 10.1016/j.physletb.2012.08.021. Cited on page 4.
- [10] Standard model of elementary particles. http://en.wikipedia.org/wiki/File:Standard_Model_of_Elementary_Particles.svg, 2014. Accessed: 2014-03-24. Cited on page 5.
- [11] G. Jungman, M. Kamionkowski, and K. Griest. Supersymmetric dark matter. *Physics Reports*, 267:195–373, March 1996. doi: 10.1016/0370-1573(95)00058-5. Cited on pages 4 and 7.

- [12] V. Trimble. Existence and nature of dark matter in the universe. *Annual Review of Astronomy and Astrophysics*, 25(1):425–472, 1987. doi: 10.1146/annurev.aa.25.090187.002233. URL <http://dx.doi.org/10.1146/annurev.aa.25.090187.002233>. Cited on page 5.
- [13] F. Zwicky. Die Rotverschiebung von extragalaktischen Nebeln. *Helvetica Physica Acta*, 6:110–127, 1933. Cited on page 6.
- [14] NASA. NASA’s solar system exploration: the planets: orbits and physical characteristics. <https://solarsystem.nasa.gov/planets/charchart.cfm>, 2014. Accessed: 2014-03-21. Cited on page 6.
- [15] T. S. van Albada, J. N. Bahcall, K. Begeman, and R. Sancisi. Distribution of dark matter in the spiral galaxy NGC 3198. *Astrophysical Journal*, 295:305–313, August 1985. doi: 10.1086/163375. Cited on page 6.
- [16] P. Gondolo. Non-baryonic dark matter. *NATO Sci.Ser.II*, 187:279–333, 2005. Cited on page 6.
- [17] J. Goodman, M. Ibe, A. Rajaraman, W. Shepherd, Tim M.P. Tait, et al. Constraints on Light Majorana dark Matter from Colliders. *Phys.Lett.*, B695:185–188, 2011. doi: 10.1016/j.physletb.2010.11.009. Cited on pages 7 and 8.
- [18] ATLAS Collaboration. Search for dark matter candidates and large extra dimensions in events with a jet and missing transverse momentum with the atlas detector. *J. High Energy Phys.*, 04(arXiv:1210.4491. CERN-PH-EP-2012-210):075. 58 p, October 2012. URL <http://cds.cern.ch/record/1485031>. Cited on pages 7 and 9.
- [19] J. Goodman, M. Ibe, A. Rajaraman, W. Shepherd, T. M. P. Tait, and H.-B. Yu. Constraints on dark matter from colliders. *Phys.Rev.D82:116010,2010*, 82(11):116010, December 2010. doi: 10.1103/PhysRevD.82.116010. Cited on page 8.
- [20] ATLAS. Atlas luminosity public results. <https://twiki.cern.ch/twiki/bin/view/AtlasPublic/LuminosityPublicResults>, 2013. Accessed: 2014-03-06. Cited on page 10.
- [21] AC Team. The four main LHC experiments, Jun 1999. URL <http://cds.cern.ch/record/40525>. Cited on page 10.
- [22] The ATLAS Collaboration. The atlas experiment at the cern large hadron collider. *Journal of Instrumentation*, 3(08):S08003. 437 p, 2008. URL <https://cdsweb.cern.ch/record/1129811/>. Cited on page 11.
- [23] J. Pequeno. Computer generated image of the whole ATLAS detector, Mar 2008. URL <http://cds.cern.ch/record/1095924>. Cited on page 12.
- [24] ATLAS Collaboration. Event display for one of the monojet candidates in the data. The event has a jet with $p_t = 602$ GeV at $\eta = -1$ and $\phi = 2.6$, $MET = 523$ GeV, and no additional jet with $p_{tjet} > 30$ GeV in the final state. . https://atlas.web.cern.ch/Atlas/GROUPS/PHYSICS/CONFNOTES/ATLAS-CONF-2011-096/fig_08.png, 2011. Accessed: 2014-03-28. Cited on page 13.
- [25] ATLAS Collaboration. Physics at a High-Luminosity LHC with ATLAS. Jul 2013. URL <https://cds.cern.ch/record/1564937>. Cited on page 15.

- [26] J. Alwall, M. Herquet, F. Maltoni, O. Mattelaer, and T. Stelzer. MadGraph 5: going beyond. *Journal of High Energy Physics*, 6:128, June 2011. doi: 10.1007/JHEP06(2011)128. Cited on pages 15 and 33.
- [27] T. Gleisberg, S. Hoeche, F. Krauss, A. Schalicke, S. Schumann, et al. SHERPA 1. alpha: A Proof of concept version. *JHEP*, 0402:056, 2004. doi: 10.1088/1126-6708/2004/02/056. Cited on pages 15 and 33.
- [28] T. Sjöstrand, S. Mrenna, and P. Skands. A brief introduction to {PYTHIA} 8.1. *Computer Physics Communications*, 178(11):852 – 867, 2008. ISSN 0010-4655. doi: <http://dx.doi.org/10.1016/j.cpc.2008.01.036>. URL <http://www.sciencedirect.com/science/article/pii/S0010465508000441>. Cited on page 15.
- [29] The ROOT Team. Root. <http://root.cern.ch/drupal/>, 2014. Accessed: 2014-03-28. Cited on page 15.
- [30] S. Agostinelli, J. Allison, K. Amako, et al. Geant4—a simulation toolkit. *Nuclear Instruments and Methods in Physics Research Section A: Accelerators, Spectrometers, Detectors and Associated Equipment*, 506(3):250 – 303, 2003. ISSN 0168-9002. doi: [http://dx.doi.org/10.1016/S0168-9002\(03\)01368-8](http://dx.doi.org/10.1016/S0168-9002(03)01368-8). URL <http://www.sciencedirect.com/science/article/pii/S0168900203013688>. Cited on page 17.
- [31] ATLAS Collaboration. Performance assumptions for an upgraded ATLAS detector at a High-Luminosity LHC. Mar 2013. URL <https://cds.cern.ch/record/1527529/>. Cited on pages 17, 18, 19, 20, 22, 28, and 29.
- [32] ATLAS Collaboration. Electron performance measurements with the ATLAS detector using the 2010 LHC proton-proton collision data. *Eur. Phys. J. C*, 72(arXiv:1110.3174. CERN-PH-EP-2011-117):1909. 45 p, Oct 2011. Comments: 33 pages plus author list (45 pages total), 24 figures, 12 tables, submitted to Eur. Phys. J. C. Cited on pages 28 and 29.
- [33] ATLAS Collaboration. Search for New Phenomena in Monojet plus Missing Transverse Momentum Final States using 10fb-1 of pp Collisions at $\sqrt{s}=8$ TeV with the ATLAS detector at the LHC. Nov 2012. URL <http://cds.cern.ch/record/1493486/>. Cited on pages 33, 34, 39, and 46.

Upphovsrätt

Detta dokument hålls tillgängligt på Internet — eller dess framtida ersättare — under 25 år från publiceringsdatum under förutsättning att inga extraordinära omständigheter uppstår.

Tillgång till dokumentet innebär tillstånd för var och en att läsa, ladda ner, skriva ut enstaka kopior för enskilt bruk och att använda det oförändrat för icke-kommersiell forskning och för undervisning. Överföring av upphovsrätten vid en senare tidpunkt kan inte upphäva detta tillstånd. All annan användning av dokumentet kräver upphovsmannens medgivande. För att garantera äktheten, säkerheten och tillgängligheten finns det lösningar av teknisk och administrativ art.

Upphovsmannens ideella rätt innefattar rätt att bli nämnd som upphovsman i den omfattning som god sed kräver vid användning av dokumentet på ovan beskrivna sätt samt skydd mot att dokumentet ändras eller presenteras i sådan form eller i sådant sammanhang som är kränkande för upphovsmannens litterära eller konstnärliga anseende eller egenart.

För ytterligare information om Linköping University Electronic Press se förlagets hemsida <http://www.ep.liu.se/>

Copyright

The publishers will keep this document online on the Internet — or its possible replacement — for a period of 25 years from the date of publication barring exceptional circumstances.

The online availability of the document implies a permanent permission for anyone to read, to download, to print out single copies for his/her own use and to use it unchanged for any non-commercial research and educational purpose. Subsequent transfers of copyright cannot revoke this permission. All other uses of the document are conditional on the consent of the copyright owner. The publisher has taken technical and administrative measures to assure authenticity, security and accessibility.

According to intellectual property law the author has the right to be mentioned when his/her work is accessed as described above and to be protected against infringement.

For additional information about the Linköping University Electronic Press and its procedures for publication and for assurance of document integrity, please refer to its www home page: <http://www.ep.liu.se/>